

Volumetric reconstruction of ionospheric electric currents from tri-static incoherent scatter radar measurements

J. P. Reistad¹, S. M. Hatch¹, K. M. Laundal¹, K. Oksavik^{1,2}, M. Zettergren³,
H. Vanhamäki⁴, and I. Virtanen⁴

¹Department of Physics and Technology, University of Bergen, Norway

²Arctic Geophysics, University Centre in Svalbard, Longyearbyen, Norway

³Physical Sciences Department, Embry-Riddle Aeronautical University, FL, USA

⁴Space Physics and Astronomy Research Unit, University of Oulu, Oulu, Finland

Key Points:

- A technique for volumetric reconstruction of 3D electric current density from tri-static incoherent scatter radar observations is presented
- Considering the anticipated noise levels, the radar system is likely to produce good current density estimates in a limited region
- The reconstruction technique is particularly well suited for inclusion of additional data sources that improve overall performance

Corresponding author: Spencer M. Hatch, spencer.hatch@uib.no

Abstract

We present a new technique for the upcoming tri-static incoherent scatter radar system EISCAT 3D (E3D) to perform a volumetric reconstruction of the 3D ionospheric electric current density vector field, focusing on the feasibility of the E3D system. The input to our volumetric reconstruction technique are estimates of the 3D current density perpendicular to the main magnetic field, \mathbf{j}_\perp , and its co-variance, to be obtained from E3D observations based on two main assumptions: 1) Ions fully magnetised above the *E* region, set to 200 km here. 2) Electrons fully magnetised above the base of our domain, set to 90 km. In this way, \mathbf{j}_\perp estimates are obtained without assumptions about the neutral wind field, allowing it to be subsequently determined. The volumetric reconstruction of the full 3D current density is implemented as vertically coupled horizontal layers represented by Spherical Elementary Current Systems with a built-in current continuity constraint. We demonstrate that our technique is able to retrieve the three dimensional nature of the currents in our idealised setup, taken from a simulation of an active auroral ionosphere using the Geospace Environment Model of Ion-Neutral Interactions (GEMINI). The vertical current is typically less constrained than the horizontal, but we outline strategies for improvement by utilising additional data sources in the inversion. The ability to reconstruct the neutral wind field perpendicular to the magnetic field in the *E* region is demonstrated to mostly be within ± 50 m/s in a limited region above the radar system in our setup.

Plain Language Summary

We introduce a novel method for the upcoming EISCAT 3D (E3D) radar system to reconstruct the 3D electric current density vector in Earth's ionosphere. Here we present the new technique and assess its feasibility for the E3D system. The input to the 3D reconstruction technique relies on estimates of the current density perpendicular to the Earth's magnetic field, obtained from the E3D observations. We include estimates of uncertainties originating from the observations of the 3D ion velocity vectors and electron density in our reconstruction. Comparisons with simulations of an active auroral ionosphere exemplify that our technique provides reasonably accurate estimates of current density, especially in the 90-150 km altitude range. Our results demonstrate success in retrieving the horizontal part of the electric current system in the *E* region, while the vertical part has more uncertainty. Our method offers insight into how electric currents flow in a specific region of the Earth's atmosphere. The results can be further improved with additional data sources; this flexibility is a significant advantage of our approach. Overall, our study facilitates the advanced knowledge of Earth's upper atmosphere using innovative radar observations in companion with advanced analysis techniques.

1 Introduction

Obtaining insights into the three-dimensional aspects of high latitude ionospheric dynamics has been a challenging task for decades (Maeda & Kato, 1966; Leadabrand et al., 1972; Brekke et al., 1974; Marklund, 1984; Brekke & Hall, 1988; Moen & Brekke, 1993; Nozawa et al., 2005). Such endeavors have mainly been motivated by improving our fundamental understanding of how the Earth's upper atmosphere is coupled to space. Recently, also the ability to predict the atmosphere responses for Low Earth Orbit operations has become urgent (e.g. Fang et al., 2022).

The complexity of considering a full 3D volume of the atmosphere is so vastly different from 1D and 2D descriptions that specialized instruments and tools are needed. In the last decade a new facility called EISCAT 3D (E3D) has been under planning (McCrea et al., 2015) and subsequent construction in northern Fennoscandia. The European Incoherent Scatter radar scientific association (EISCAT) has operated incoherent scatter radars (ISR) in the European arctic sector since 1981 (Rishbeth, 1982). With E3D a new

generation multi-site phased-array radar system is introduced. The agile technical design allows the system to be used for volumetric measurements by means of multiple simultaneous receiver beams and rapidly scanning the transmitter and receiver beam directions. Furthermore, the tri-static system is expected to facilitate measurements of the full 3D ion velocity in coordinated operations (e.g. Stamm et al., 2021).

This paper targets an investigation of the capabilities of E3D to reconstruct the 3D electric current density in a volume above the radar system, a key scientific goal of the E3D radar system (McCrea et al., 2015). Electric currents are key quantities in ionospheric plasma and closely linked to magnetic perturbations observed from ground or space. Electric currents also offer insights into 3D energy deposition through plasma interactions with the neutral atmosphere. Fully understanding the physical processes in this region of space, where complex atmosphere-space interactions take place, relies on major advances in both instrumentation and analysis methodology. The latter is the target of this paper, to develop new analysis tools that facilitate ground-breaking new insights from E3D observations and similar instrumentation. In this paper we present an Observing System Simulation Experiment (OSSE) of the process of volumetric reconstruction of the electric current density from E3D-like observations. The OSSE method has proven effective to map the impact of the observing system design on its performance (e.g. Laundal et al., 2021), and is used here to gain insights into how the E3D system can be applied in an effective way to obtain estimates of the electric current density in the region above the radar system.

Stamm et al. (2023) recently presented a technique with strong parallels to our work. They explored the capabilities of using E3D observations to simultaneously estimate both the ionospheric electric field and neutral wind field. Two of the most important distinctions between the two approaches are that we assume the electrons are magnetized all the way down to the base of the analysis region, which is 90 km in our case, and we assume that the electric field may be represented by a two-dimensional electric potential. Stamm et al. (2023) make neither of these assumptions explicitly; they instead apply additional constraints to their solution through regularization, based on physical principles (see Section 3 and Equation 21 in their study). The work presented in our paper complements the work by Stamm et al. (2023) with an alternative approach to derive similar quantities from the upcoming E3D facility. Of special significance is the similarity our approach bears to the Local mapping of polar ionospheric electrodynamics (Lompe) data assimilation technique (Laundal et al., 2022), allowing for convenient integration of various additional data sources into the reconstruction process. As will be shown in section 5, additional data can improve the reconstruction significantly, leading to more realistic results in a larger part of the volume.

The remainder of this paper describes a technique that utilise the information obtained from observing the incoherent scatter spectrum to produce volumetric estimates of the 3D electric current density. Figure 1 is a flowchart of the different steps involved, to be presented in more detail throughout this paper. The input to our processing is shown in yellow boxes in Figure 1. Section 2 describes in detail how our pre-processing (purple boxes) of these input lead to estimates of the current density perpendicular to the main magnetic field, \mathbf{j}_\perp at the measurement locations, which is the input to the volumetric reconstruction technique that we call **E3DSECS**, introduced in section 3. Section 4 presents the performance of our technique, followed by suggestions for how this can be improved in section 5. Finally, we provide some concluding remarks in section 6.

2 Estimating \mathbf{j}_\perp with EISCAT 3D

The current density is not one of the primary parameters deduced from the ion line ISR spectrum, so additional assumptions must be made. This section describes how we can arrive at estimates of \mathbf{j}_\perp in a two-step process. First, the ionospheric convection elec-

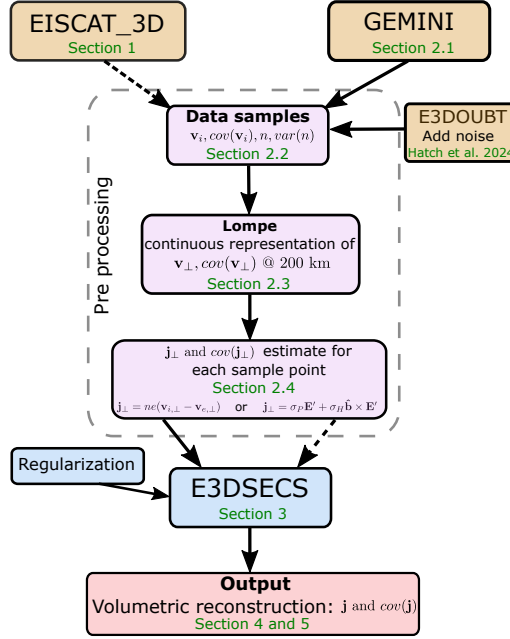


Figure 1. Flowchart of the different steps involved in the volumetric reconstruction of the electric current density \mathbf{j} . Respective section numbers are indicated in green color. Inputs to our processing are indicated with yellow, processing steps in purple, and output in pink.

tronic field \mathbf{E}_\perp is estimated from E3D observations at altitudes where ion-neutral interactions can be neglected, described in section 2.3. Subsequently, two possible approaches are outlined that both give estimates of the perpendicular current density \mathbf{j}_\perp from E3D measurements. Both methods utilise the assumption of the perpendicular electron motion being frozen-in all the way down to the bottom of the 3D domain. The resulting \mathbf{j}_\perp estimates (both methods explained in section 2.4) form the basis for the volumetric reconstruction method of the full 3D current density vector \mathbf{j} based on current continuity, to be further described in section 3.

2.1 Means of validation: GEMINI model

For the development of the volumetric reconstruction method of the 3D ionospheric current density based on E3D observations, a realistic set of synthetic data is needed as a “ground truth” baseline for the reconstruction results. We use outputs from the Geospace Environmental Model of Ion-Neutral Interactions (GEMINI) (Zettergren & Snively, 2015; Zettergren, 2019) for this purpose. GEMINI computes self-consistent solutions to the ionospheric plasma continuity, momentum, and energy equations (including chemical and collisional sources) and is coupled to a quasistatic description of ionospheric current closure which provides a solution for the ionospheric electric potential given an input field-aligned current. For brevity we omit a full description of the governing equation in GEMINI as these are listed and described in detail in Appendix A of Zettergren and Snively (2015).

The GEMINI simulation used in the present study includes a pair of static up/down field aligned currents (FAC) above Northern Fennoscandia, oriented along magnetic (dipole) parallels as seen in Figure 2. All analysis presented here is based on the last time step in the simulation, made available together with this publication (Reistad & Zettergren, 2024). Red color indicates a current out of the ionosphere. The electric potential at 200

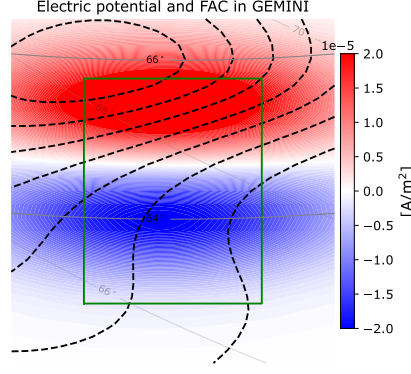


Figure 2. The GEMINI model is forced with a pair of up/down field aligned currents, here shown as red/blue colors, respectively. The electric potential from GEMINI is shown as dashed black contours at 3 kV intervals. The field aligned current pattern is aligned in the magnetic east/west direction, indicated by the grey magnetic dipole latitude parallels (geographic latitude contours are also shown for reference, in lighter grey). The 200 km altitude footprint of the volumetric reconstruction region used throughout this paper is indicated in green, approximately aligned with the magnetic latitude contours.

km altitude is shown as dashed black lines with 3 kV intervals. In the simulation the neutral atmosphere is stationary in the frame of the Earth.

2.2 Sampling from the GEMINI model output and adding realistic noise

We have chosen to sample from the GEMINI simulation at 103 altitudes along 31 beams. The beam configuration consists of 3 “rings” of 10 beams each, uniformly separated in azimuth, see Figure 6. The elevation angles of the rings are 55°, 65°, and 75°. The last beam is vertical. Each site of the E3D system (one transceiver and two dedicated receivers) is located approx. 200 km south compared to its real locations to probe a more relevant part of the simulation output, covering the transition between the up and down FAC regions, see Figure 2. Samples of electron density and 3D ion velocities are retrieved along the beams between 90 and 500 km altitude in 4-km altitude intervals, leading to a total of 3,133 observations. The modeled values from GEMINI are estimated at these locations from linear interpolation from the native GEMINI grid which has a spatial resolution of approx. 5 km in the vertical and north-south direction, and approx. 15 km in the east-west direction in our region of interest.

To yield a more realistic case for investigating the performance of the volumetric E3D based 3D reconstruction, we added noise to the observed 3D ion velocities \mathbf{v}_i and electron density n . The variances and co-variances of the observed n and \mathbf{v}_i are estimated based on the specified beam configuration, integration time (10 min total, approximately 19.4 s per beam), electron density, electron and ion temperature (taken from GEMINI), and a reference atmosphere. These calculations are carried out using the *e3doubt* package (Hatch & Virtanen, 2024).

2.3 Estimating \mathbf{v}_\perp at a reference altitude

In both of the approaches to estimate \mathbf{j}_\perp outlined in section 2.4, we make the convenient assumption that the electron mobility $k_e = \frac{\Omega_e}{\nu_{en}} \gg 1$ all the way to the base of our volume, set to 90 km in the example to be shown. Here, Ω_e and ν_{en} are the electron gyro-frequency and electron-neutral collision frequency, respectively. We likewise

assume that the electric field maps along field lines everywhere within the reconstruction domain. This is a reasonable assumption for the scale sizes addressed in this study (of order 10s of km, see Farley, 1959). With this assumption the electron motion perpendicular to \mathbf{B} in the lower parts of our domain directly follows from the ion motion in the higher parts where the ion mobility $k_i = \frac{\Omega_i}{\nu_{in}} \gg 1$. This assumption ($k_e \gg 1$) is a much used simplification above 100 km (Boström, 1964; Kaeppler et al., 2015) that greatly reduces the complexity of the 3D reconstruction technique.

As mentioned in the introduction, we further assume that the convection electric field is a potential field, $\mathbf{E} = -\nabla\Phi$. Hence, we neglect the contribution from compressional flows related to dynamic processes changing the magnetic field through induction (see e.g. Vanhamäki et al., 2007; Madelaire et al., 2024). The use of a potential electric field may not be valid for combining velocity estimates obtained using short integration times, and during very active conditions such as sudden commencements. However, for this application, several minutes of integration time is likely needed to sample the volume with a large number of beams.

Estimating the electric potential Φ (used to express \mathbf{v}_\perp in our domain) may be done in a completely separate process from the volumetric 3D reconstruction of the current density field, which is our primary goal. With E3D, the convection electric field can be estimated by combining all 3D ion velocities in the domain above a height h_Φ where ion-neutral interactions are assumed to be negligible. We have used $h_\Phi = 200$ km in our tests with GEMINI outputs. To estimate Φ it would be beneficial to place h_Φ as low as possible. A low h_Φ will improve the spatial coverage, as each observation will sample a new field line. In principle, any other relevant observation of the F -region plasma flow may be used to improve the estimate, such as Doppler shift velocities from ground based HF radars. Before fitting Φ at h_Φ , we map the observed 3D ion velocities (from E3D) between h_Φ and 500 km to h_Φ using eq. 4.17 in Richmond (1995) and Modified Apex basis vectors with a reference height of 110 km (sometimes referred to as MA-110 coordinates). Since GEMINI uses a centered dipole main field, we use the dipole equivalents of the Modified Apex base vectors (Laundal, 2024). Then, we use the Local Mapping of Polar ionospheric Electrodynamics (Lompe) (Laundal et al., 2022; Hovland et al., 2022) framework to represent Φ . The use of Lompe is a matter of convenience, as it offers the relevant grid and interpolation functionality, and uses the assumption of a potential electric field to constrain the fit of the input data.

The Lompe representation of Φ is by design made to express a purely horizontal E-field, which is the projection of the actual \mathbf{E} that is assumed to have no component along \mathbf{B} , namely $\mathbf{E} = -\nabla\Phi = -\mathbf{v} \times \mathbf{B}$. Therefore, the parallel component of the sampled ion velocity \mathbf{v}_i is removed as part of the mentioned mapping, and only the horizontal components (east, north) of the mapped $\mathbf{v}_{i,\perp}$ is used as input to the Lompe-fit. However, when evaluating the Lompe-description of the convection, the radial part of \mathbf{v}_\perp is recovered by invoking $\mathbf{v}_\perp \cdot \mathbf{B} = 0$. This is relevant since the field inclination above the E3D facility is approximately 11° . Hence, the E-field used in the subsequent reconstruction is the full \mathbf{E}_\perp , and not only its horizontal projection.

An example of the Lompe fit is shown in Figure 3. Here, the mapped $\mathbf{v}_{i,\perp}$ vectors are shown at the h_Φ height as orange vectors, representing the input data used in Lompe. The noise added into the observations is evident, as the underlying GEMINI simulation is as smooth as the electric potential pattern shown in Figure 2. The resulting fitted convection velocities are shown as black arrows, and the electric potential as blue contour lines (5 kV intervals). To reduce artifacts close to the perimeter of the Lompe representation, only the interior part inside the green rectangle is used for the subsequent volumetric reconstruction. This is the same green frame used in all subsequent figures throughout this paper, and has a horizontal extent of approx. 300×300 km, with edges of approx. 20 km, see Figure 7 and section 3.2 for details. The performance of the Lompe-fit inside this interior region is seen in the right panel. Here, a uniform mesh of points

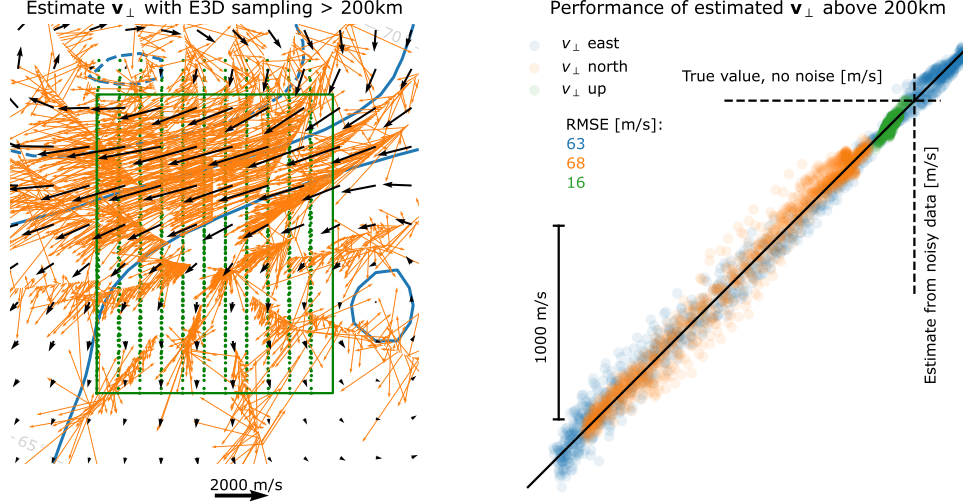


Figure 3. Left: Lompe is fitted with horizontal part of $\mathbf{v}_{\perp,i}$ above h_{Φ} , after being mapped down to h_{Φ} , here shown with orange vectors. The jitter seen in the observations originate from the noise that has been added (see section 2.5 for details). Black vectors and blue contours show the Lompe output velocity and electric potential, respectively. Right: The GEMINI model is evaluated on a uniform 3D mesh between $h_{\Phi} = 200$ km and 500 km above the interior region. Green dots in left panel represents the sampling locations mapped down to h_{Φ} . A good agreement between the mapped $\mathbf{v}_{\perp,i}$ from GEMINI (without noise) and \mathbf{v}_{\perp} from Lompe (based on noisy observations) is demonstrated.

is sampled from the GEMINI model, extending in altitude in 7 layers from h_{Φ} up to 500 km, referred to as “evaluation locations”. The evaluation locations mapped down to h_{Φ} are indicated with green dots in the left panel. The perpendicular ion velocities $\mathbf{v}_{i,\perp}$ from GEMINI (with no noise added) at the evaluation locations are also mapped down to h_{Φ} , facilitating a direct comparison to what is estimated with the Lompe representation at the same locations. The right panel in Figure 3 shows this performance. In this example, a fair correspondence is seen in all three components of \mathbf{v}_{\perp} for this 31-beam configuration; at the same time the deviations of the magnitudes of the estimated \mathbf{v}_{\perp} are > 100 m/s for typically 30% of the evaluation locations. The performance of the \mathbf{v}_{\perp} reconstruction with Lompe also depends on the degree of structure in the convection field that is being mapped, where more structure requires a larger number of beams to capture the variation. The main sources for the deviations from the black line in this example is expected to originate from the sparseness in observation density above 200 km in our beam configuration, and the estimated noise from the tri-static E3D system.

2.4 Inferring \mathbf{j}_{\perp} from ISR measurements

Using the definition of electric current density

With E3D, we expect to obtain 3D vector estimates of \mathbf{v}_i within the field of view (FOV) above the radar. The perpendicular current density \mathbf{j}_{\perp} can thus be estimated when $\mathbf{v}_{e,\perp}$ is specified, from the differential motion of ions and electrons:

$$\mathbf{j}_{\perp} = ne(\mathbf{v}_{i,\perp} - \mathbf{v}_{e,\perp}) \quad (1)$$

where n is the electron density (also observed with E3D), and e is the elementary charge. With the continuous description of \mathbf{v}_{\perp} at h_{Φ} (using Lompe), we can now evaluate for

\mathbf{v}_\perp at the locations at h_Φ that map to each observation along our beams (and also any other location within the domain). Due to our assumption of frozen-in electrons, this mapping allows us to express the perpendicular electron velocity $\mathbf{v}_{e,\perp}$ at each measurement location along our beams purely based on the estimated 2D electric potential Φ . Thus, by applying equation 1 we can obtain estimates of the perpendicular current density at each E3D sample location. Because of our above assumptions about negligible ion-neutral interactions above h_Φ , our \mathbf{j}_\perp estimates from equation 1 is only valid below this altitude. Note that despite the perpendicular current arising from interactions with the neutral atmosphere, the current density is a frame invariant quantity in Galilean relativity (Mannucci et al., 2022). Hence, the currents estimated in this way (not using any assumptions about the neutral wind field) can in principle be used to further constrain the neutral wind field in the regions of ion-neutral interactions. We return to this in section 6.

The performance of this method is illustrated in Figure 4. Here we can see the geographic eastward (ϕ) component of \mathbf{j}_\perp in color on a north-south slice inside the 3D volume from which we assume we can get ion velocity vector measurements from E3D. The left panel shows the quantity as represented in the GEMINI model (the ground truth with no noise), interpolated to our sampling grid (what is indicated by the vertical slice). A set of field-lines (orange) are also shown originating from the edge of the data-cube that faces towards magnetic north. A horizontal grey line is shown at $h_\Phi = 200$ km to illustrate the region where ions are assumed to not interact strongly with the neutral atmosphere, and our estimates using equation 1 should be valid. An eastward current (red) is seen in the E region toward the northern part of the domain, corresponding to the region of strong westward convection seen in Figures 2 and 3, indicating a Hall current. The middle panel shows the estimated perpendicular eastward current density from the method outlined above. It must be mentioned that in Figure 4, no noise has been added to the \mathbf{v}_i samples in the slice shown. We here show samples from a uniform grid in the slice shown, not corresponding to a typical beam configuration, which is what `e3doubt` needs to estimate the variances. Hence, this figure reflects purely the ability of the estimated convection electric field (estimated using a realistic beam configuration and noise) to estimate \mathbf{j}_\perp when combined with the assumption of frozen-in electron motion. In section 2.5 we show how the uncertainties estimated with `e3doubt` for our 31-beam setup propagate into uncertainties in the estimated \mathbf{j}_\perp by also taking into account the covariance of the measured \mathbf{v}_i and the variance in n in equation 1, which should be representative for the errors of the estimates in Figure 4.

The agreement of the estimated $\mathbf{j}_{\perp,\phi}$ in Figure 4 is mostly good in the E region where the perpendicular current is significant and the use of equation 1 is valid, highlighted by the difference plot to the right. Here, the reconstructed $\mathbf{j}_{\perp,\phi}$ is mostly within $\pm 20\%$ of the ground truth. This is also the case for the northward component of the current (not shown). Most notable are the differences above the strong horizontal currents. Here, a slight error in the modelled $\mathbf{v}_{e,\perp}$ introduces an erroneous $j_{\perp,\phi}$, highlighting the challenge of representing the difference between two large quantities (catastrophic cancellation). Even though we will not use \mathbf{j}_\perp estimates above h_Φ , this effect increases the errors also in the E region. In the remainder of this subsection we elaborate on an alternative approach to estimate \mathbf{j}_\perp that may be beneficial with respect to this challenge.

Using the ionospheric Ohm's law to represent \mathbf{j}_\perp

As an alternative to using the difference between ion and electron velocity to estimate the current density, the ionospheric Ohm's law (hereafter simply "Ohm's law") can be used. Ohm's law describes the steady state relationship between the convection electric field in the reference frame of the neutral atmosphere, the current density, and the ionospheric Hall and Pedersen conductivity, σ_H and σ_P :

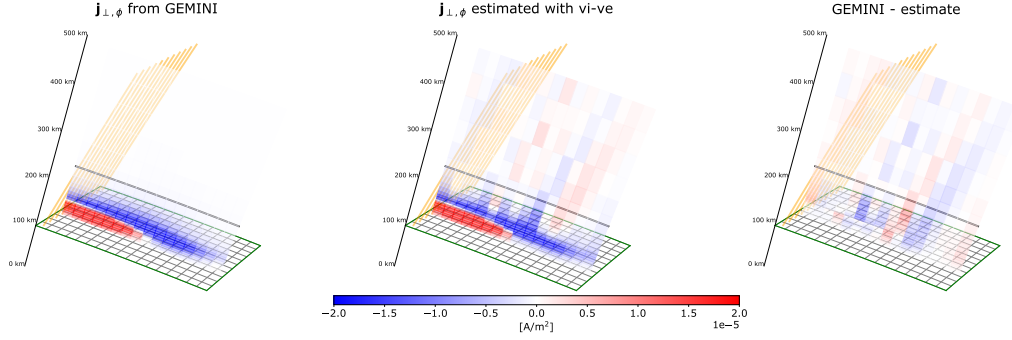


Figure 4. Geographic eastward component of \mathbf{j}_\perp in color shown on a vertical slice through the data-cube to be used in the volumetric reconstruction of the 3D \mathbf{j} described in the next section. Left: Output from the GEMINI model (no noise), which is what we try to represent using our estimate of the convection electric field. Middle: The same quantity recreated using the velocity difference between ions and electrons. Right: The difference. Field lines originating from the bottom edge of the northward facing side of the data cube is shown in orange. Lompe grid at 90 km is shown in green, and the mapping altitude $h_\Phi = 200$ km is indicated with a horizontal grey line. Due to our frozen in assumptions, \mathbf{j}_\perp estimates above h_Φ is not used in our subsequent analysis.

$$\mathbf{j}_\perp = \mathbf{j}_P + \mathbf{j}_H = \sigma_P \mathbf{E}' + \sigma_H \hat{\mathbf{b}} \times \mathbf{E}' \quad (2)$$

where $\hat{\mathbf{b}}$ is a unit vector along the main magnetic field \mathbf{B} . The two terms are referred to as the Pedersen and Hall current. $\mathbf{E}' = \mathbf{E} + \mathbf{u} \times \mathbf{B}$ is the electric field in the frame of the neutral wind \mathbf{u} . In the GEMINI simulation used here, $\mathbf{u} = 0$, meaning that the neutral atmosphere co-rotates with the surface. In reality, \mathbf{u} can be of relevance and have significant vertical velocity shears in the E region (Larsen, 2002; Sangalli et al., 2009).

By assuming a neutral wind field, equation 2 can be used to estimate \mathbf{j}_\perp if the conductivity is also known. Since E3D will get simultaneous measurements of the electron density and ion temperature, σ_H and σ_P can be estimated based on assumptions of the neutral atmosphere density and temperature profile (to obtain estimates of ion-neutral collision frequency at measurement locations). In this approach, one is guaranteed to get small \mathbf{j}_\perp estimates at high altitudes due to the low conductivity, which the velocity difference approach struggles with due to the catastrophic cancellation effect. However, the Ohm's law approach builds upon assumptions about the neutral atmosphere density, temperature, and winds that are not imposed in the velocity difference method.

Figure 5 shows the estimated perpendicular eastward current density using the Ohm's law approach outlined here, in the same format as Figure 4. This is expected to work very well since $\mathbf{u} = 0$ is used in the GEMINI simulation. Furthermore, the conductivity is known precisely as this is also derived from the GEMINI simulation output. An interesting aspect of the Ohm's law approach is that it may offer an advantageous way to incorporate additional information about the neutral atmosphere. Since the number of beams available is highly restricted compared to the vast volume of the reconstruction region, additional information is most likely needed to constrain the volumetric reconstruction of \mathbf{j} to produce physically meaningful results. This we return to in section 5.

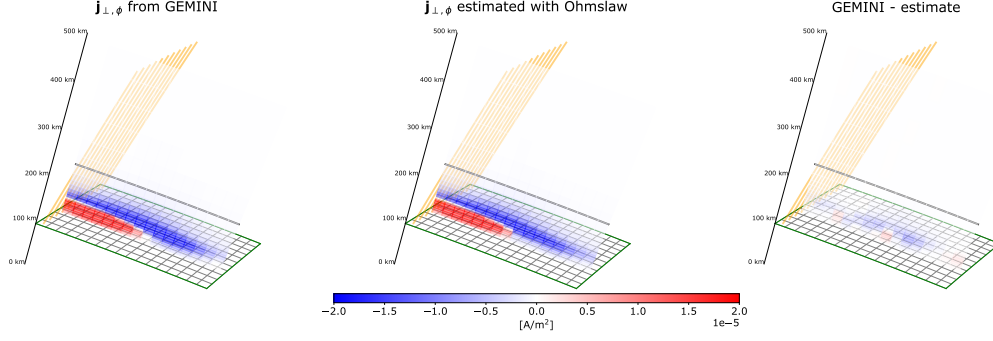


Figure 5. Estimates of the eastward component of the perpendicular current density based on the estimated convection electric field and knowledge about the ionospheric conductivity using the ionospheric Ohm’s law. The format is the same as Figure 4.

2.5 Uncertainty estimates

We here perform a rough estimate of the expected errors due to the process of observing the incoherent scatter spectrum with E3D. We use the default E3D configuration of the `e3doubt` package, aside from shifting the three E3D sites 200 km to the south as described in section 2.2, setting the range resolution to 4 km, and specifying a total integration time of 10 min.

By default `e3doubt` uses a 233 MHz carrier frequency, 3.5 MW transmitter power, 25 % duty cycle, and 300 K system noise temperature for all receivers. The transmission and reception beam widths at the core transceiver site are 2.1° and 1.2° , respectively, and the remote receiver sites have 1.7° beam width. The core site transmission and reception beams have different widths, because transmitters will not be installed to all core site antenna elements in the first phase of E3D.

The `e3doubt` package uses the GEMINI simulation plasma parameters and radar equation to calculate signal power and incoherent scatter self-noise power in each receiver beam. These powers are then converted into noise levels of the decoded lag profiles and subsequently to standard deviations of the fitted plasma parameters following the scheme presented by Vallinkoski (1988). Standard deviations of the ion velocities as observed at the three receiver sites are then used to calculate the 3x3 covariance matrix for each 3D observation of the ion drift velocity vector from the E3D system, $cov(\mathbf{v}_i)$. By utilizing the Apex base vectors $\mathbf{d}_1, \mathbf{d}_2, \mathbf{e}_1$, and \mathbf{e}_2 , the mapping of the perpendicular part of the 3D ion velocity measurements above h_Φ (\mathbf{v}_i) down to this altitude (\mathbf{v}_m) can be represented as the operation

$$\mathbf{v}_m = \mathbb{M}\mathbf{v}_i. \quad (3)$$

where \mathbb{M} is the mapping matrix made from the Apex basis vectors. The mapping of the covariance of a vector \mathbf{v}_i when acted upon by an operator \mathbb{M} is (e.g. Aster et al., 2018)

$$cov(\mathbf{v}_m) = cov(\mathbb{M}\mathbf{v}_i) = \mathbb{M}cov(\mathbf{v}_i)\mathbb{M}^T. \quad (4)$$

This is how \mathbb{M} is used to estimate the data covariance matrix ($\mathbb{C}_d = cov(\mathbf{v}_m)$) of the mapped perpendicular 3D ion velocity observations that is used to constrain the Lompe representation of the horizontal potential electric field (see Laundal et al. (2022) for further details of the Lompe inversion). The covariance matrix of the model parameters describing the Lompe representation (\mathbf{m}_L) is given by the Lompe matrices involved in the inversion for the model parameters, namely

$$cov(\mathbf{m}_L) = (\mathbb{G}_L^T \mathbb{C}_d^{-1} \mathbb{G}_L + \mathbb{R})^{-1} \quad (5)$$

where \mathbb{G}_L is the Lompe design matrix describing how the Lompe model parameters relate to the observations of the horizontal part of \mathbf{v}_\perp (see e.g. Madelaire et al., 2023). \mathbb{R} is the regularization used when inverting for \mathbf{m}_L (here we use $\lambda_1 = 0.6, \lambda_2 = 0$ as defined in Laundal et al. (2022), determined using cross validation by minimising the residual norm). Due to the imposed regularization, there is a chance that the solution \mathbf{m}_L is biased. Thus, $cov(\mathbf{m}_L)$ could be an underestimate of the true error (including both statistical uncertainty and bias) of the convection representation if the imposed regularization is not well justified. As shown in this example, the known convection field varies smoothly, and hence we argue that our regularization is reasonable. However, in the real application to E3D the situation may be different.

The covariance of the Lompe representation is propagated further, into the perpendicular velocity at the original 3D ion velocity observation below h_Φ , which would represent the $\mathbf{v}_{e,\perp}$ estimate. This is a relevant quantity when we want to evaluate the difference between the perpendicular ion and electron velocities at each observation location to express the perpendicular current density. Going from $cov(\mathbf{m}_L)$ to $cov(\mathbf{v}_{e,\perp})$ is done in two steps, both using equation 4. First, we use the matrix \mathbb{G}_L that relates \mathbf{m}_L to \mathbf{v}_\perp at h_Φ at the locations mapping to the observations (here $\mathbf{v}_\perp \cdot \mathbf{B} = 0$ is utilized to expand \mathbb{G}_L to get the radial component of \mathbf{v}_\perp). Second, when the covariance of \mathbf{v}_\perp at h_Φ is known, \mathbf{v}_\perp is finally mapped back to its original measurement altitude to obtain the $\mathbf{v}_{e,\perp}$ estimate. The square root of the diagonal elements of $cov(\mathbf{v}_{e,\perp})$ indicate an uncertainty mostly in the range 120 – 230 m/s for the horizontal components and 30 – 60 m/s for the vertical component.

When using the velocity difference expression in equation 1, the covariance of \mathbf{j}_\perp can be expressed as

$$cov(\mathbf{j}_\perp) = e^2 [var(n) [cov(\Delta\mathbf{v}_\perp) + \Delta\mathbf{v}_\perp \Delta\mathbf{v}_\perp^T] + n^2 cov(\Delta\mathbf{v}_\perp)] \quad (6)$$

where $\Delta\mathbf{v}_\perp = \mathbf{v}_{i,\perp} - \mathbf{v}_{e,\perp}$ is the 3D vector of ion and electron perpendicular velocity difference, e is the elementary charge, and $var(n)$ is the variance of the electron density, also obtained from `e3doubt`. One can see that the covariance of \mathbf{j}_\perp does not only depend on the (co)variances of n and $\Delta\mathbf{v}_\perp$, but also scales with the electron density squared and the outer product $\Delta\mathbf{v}_\perp \Delta\mathbf{v}_\perp^T$.

Figure 6 shows to what accuracy E3D may be capable of estimating \mathbf{j}_\perp with the velocity difference method. We note that this is an estimate using a simulated event with both significant electron density and electric currents, with fairly smooth variations in space (Figure 2) and no variation in time. The performance of the actual E3D radar system will largely depend on the specific situation and operating mode. Nevertheless, the uncertainty analysis carried out here should provide some insights into the expected performance. Figure 6A shows the geographic eastward component (ϕ) of the perpendicular current density from the GEMINI model along the 31 beams. The horizontal grid within the green frame is placed at 90 km, and represents the horizontal part of the grid to be used in the volumetric reconstruction described in the following section, and is the same as the green frame in Figure 3. Panel B shows the square root of the diagonal element of $cov(\mathbf{j}_\perp)$ from equation 6 corresponding to the eastward direction. One can see that the estimated uncertainties of \mathbf{j}_\perp are substantial, with the majority of the values in the range 5-20 $\mu A/m^2$ in this example. The uncertainty of the northward component of \mathbf{j}_\perp is found to be of similar magnitudes (not shown). In Figure 6D we show the signal to noise ratio: the magnitude of the perpendicular current density from GEMINI over the magnitude of the error: $SNR = |\mathbf{j}_\perp|/|\sigma_{\mathbf{j}_\perp}|$, where $|\sigma_{\mathbf{j}_\perp}| = \sqrt{cov(\mathbf{j}_\perp)_{ee} + cov(\mathbf{j}_\perp)_{nn} + cov(\mathbf{j}_\perp)_{uu}}$, and the subscripts refer to the respective diagonal elements. Here it is evident that in the E region, the uncertainty is typically smaller than the current density itself, suggesting that it is possible to retrieve the quantity here. In Figure 6C, we plot a vertical profile along one of the beams used. One can see that below ~ 140 km, SNR is above 1. The vertical profile of $|\mathbf{j}_\perp|$ from the GEMINI model along the same beam is also shown. One can see that $|\mathbf{j}_\perp|$ is mainly confined below 140 km.

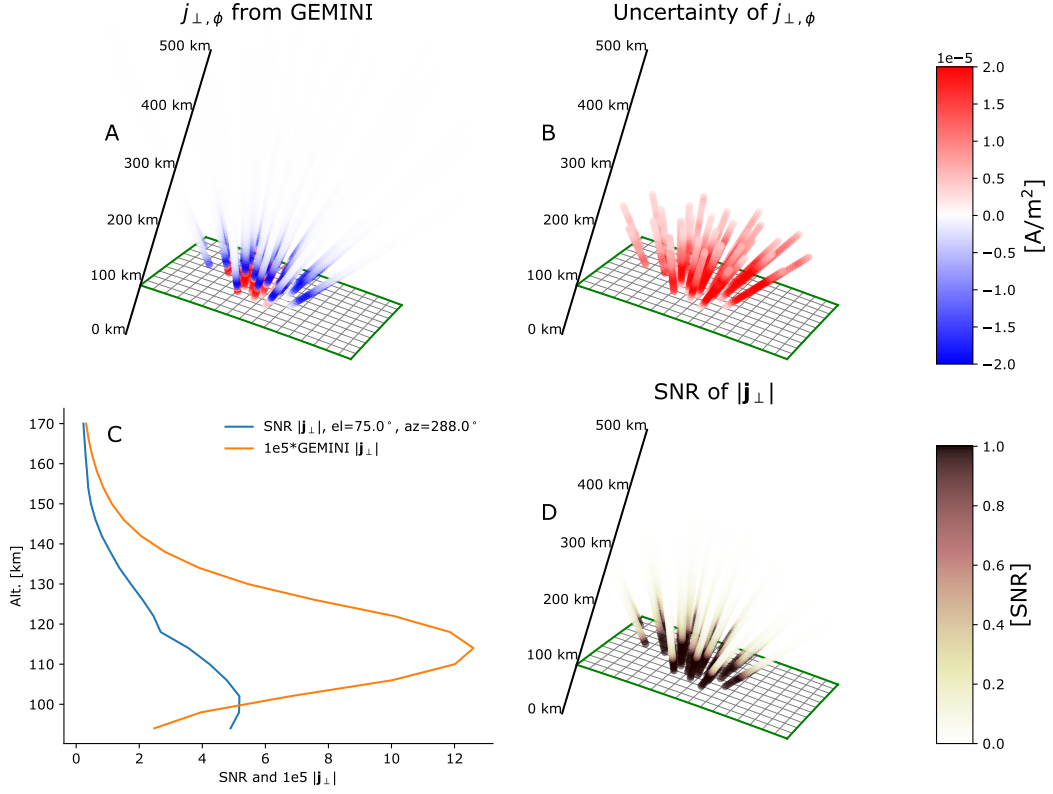


Figure 6. Co-variances of tri-static ion velocity measurements from E3D, as estimated by *e3doubt*, propagated into covariance of the estimated \mathbf{j}_{\perp} as described in section 2.5. A: The ground truth for comparison, as obtained from the GEMINI model. B: Uncertainty of $\mathbf{j}_{\perp, \phi}$, obtained as the square root of the corresponding diagonal elements of the covariance matrix. C: A vertical profile along a specific beam: Blue line is the ratio $SNR = |\mathbf{j}_{\perp}|/|\sigma_{\mathbf{j}_{\perp}}|$, showing that the error is mainly less than $|\mathbf{j}_{\perp}|$ within the *E* region. Orange line is $|\mathbf{j}_{\perp}|$ along the same beam for comparison. D: The same value as the blue line in C for all beams.

3 Volumetric reconstruction of full current density vector from \mathbf{j}_\perp observations

The motivation for this paper is to investigate the feasibility of utilizing measurements from the tri-static E3D facility to obtain a volumetric representation of the electric current density within the E3D FOV, the E3DSECS model. The above description of how to obtain estimates of \mathbf{j}_\perp and $cov(\mathbf{j}_\perp)$ is the first step of this task. We here describe a framework that enables the \mathbf{j}_\perp measurements to be used in a volumetric reconstruction of the full 3D current density (the blue boxes in Figure 1). The most fundamental physical aspects of the E3DSECS modelling scheme is presented in this section. For a detailed description of the numerical implementation, also made available as a Python package (Reistad et al., 2024), we refer the reader to Appendix A.

3.1 Decomposing the current

Since the magnetic field inclination in the E3D field of view is significant (approximately 11°), the main magnetic field should not simply be assumed to be vertical. Here we formulate how the local magnetic field orientation is used in the transformations between the full vector description of \mathbf{j} and its projection to the plane perpendicular to \mathbf{B} .

One way to decompose the current is in terms of perpendicular and field-aligned components, similar to what was done in equation 1:

$$\mathbf{j} = j_\parallel \hat{\mathbf{b}} + \mathbf{j}_\perp, \quad (7)$$

where

$$\mathbf{j}_\perp = \hat{\mathbf{b}} \times (\mathbf{j} \times \hat{\mathbf{b}}). \quad (8)$$

Another way to decompose the current is in terms of horizontal and vertical components:

$$\mathbf{j} = j_r \hat{\mathbf{r}} + \mathbf{j}_h, \quad (9)$$

where

$$\mathbf{j}_h = \hat{\mathbf{r}} \times (\mathbf{j} \times \hat{\mathbf{r}}) = j_\theta \hat{\boldsymbol{\theta}} + j_\phi \hat{\boldsymbol{\phi}}. \quad (10)$$

Here $\hat{\mathbf{r}}$ is a vertical unit vector, and $\hat{\boldsymbol{\theta}}$ and $\hat{\boldsymbol{\phi}}$ are unit vectors in the co-latitude and azimuthal directions, respectively.

If $\hat{\mathbf{b}}$ is vertical, the perpendicular/field-aligned decomposition and horizontal / vertical decompositions are identical. However, for E3D, the inclination should be taken into account. We define $\hat{\mathbf{b}} = b_r \hat{\mathbf{r}} + b_\theta \hat{\boldsymbol{\theta}} + b_\phi \hat{\boldsymbol{\phi}}$ and $\mathbf{j} = j_r \hat{\mathbf{r}} + j_\theta \hat{\boldsymbol{\theta}} + j_\phi \hat{\boldsymbol{\phi}}$. Then \mathbf{j}_\perp can be expressed as

$$\mathbf{j}_\perp = \hat{\mathbf{b}} \times (\mathbf{j} \times \hat{\mathbf{b}}) \quad (11)$$

$$= \begin{pmatrix} b_\theta^2 + b_\phi^2 & -b_r b_\theta & -b_r b_\phi \\ -b_r b_\theta & b_r^2 + b_\phi^2 & -b_\theta b_\phi \\ -b_r b_\phi & -b_\theta b_\phi & b_r^2 + b_\theta^2 \end{pmatrix} \begin{pmatrix} j_r \\ j_\theta \\ j_\phi \end{pmatrix} \quad (12)$$

$$= \mathbb{B} \mathbf{j} \quad (13)$$

where the three components refer to the r, θ, ϕ directions, here radial, co-latitude and azimuthal, respectively. The 3×3 matrix \mathbb{B} describes the projection of a vector representation of \mathbf{j} onto the plane perpendicular to \mathbf{B} , and will be used in the implementation of the 3D reconstruction of \mathbf{j} described below.

3.2 The proposed 3D representation

We now develop a horizontally layered description of the current density field by expanding a commonly used representation of the high latitude ionospheric currents. Amm

(1997) showed that the divergence-free (DF) and curl-free (CF) Spherical Elementary Current Systems (SECS) form a complete basis for describing any sufficiently smooth 2D vector field on a sphere. He also highlighted certain physical properties of CF and DF SECS that are convenient for representing currents, such as their localized nature, and that the SECS node coefficient in his 2D application has units of Ampere, representing the amount of electric current entering/leaving the localized region. The SECS representation has been widely applied to both height integrated ionospheric currents (e.g. Vanhamäki & Juusola, 2020), ionospheric convection (Amm et al., 2010; Reistad et al., 2019), and a combination thereof (Laundal et al., 2022), but to our knowledge not yet for 3D electric current densities.

In our layered representation we use the following decomposition of \mathbf{j} at each altitude layer:

$$\mathbf{j} = j_r \hat{\mathbf{r}} + \mathbf{j}_h = j_r \hat{\mathbf{r}} + \mathbf{j}^* + \mathbf{j}^\circ \quad (14)$$

where $*$ and $^\circ$ refer to the CF and DF part of \mathbf{j}_h at a given height. This is a Helmholtz decomposition, here applied to 2D spherical surfaces, enabling \mathbf{j}_h to be described with CF + DF SECS. Note that this layered description is different from the usual SECS representation, in the sense that the SECS basis functions in each layer represent the current density [A/m²] at that layer, and not a sheet current density [A/m] which is usually the case. Hence, the SECS model coefficients have units of A/m, and the sheet current density of each layer can be obtained by multiplying by the distance between layers.

The layers of CF + DF SECS describe only the horizontal part of the full current density vector. To couple the radial part of the current density with the SECS representation we impose current continuity, leading to an integral in the radial direction for j_r . Applying $\nabla \cdot \mathbf{j} = 0$ and setting $j_r(r_0) = 0$ we get

$$j_r(r) = - \int_{r_0}^r \nabla \cdot \mathbf{j}_h dr, \quad (15)$$

where in practice the integrand $\nabla \cdot \mathbf{j}_h$ is expressed in terms of height-dependent CF SECS amplitudes, since the CF amplitudes have the property that they are proportional to the divergence. The DF part of the field has by definition no divergence and therefore does not have a direct relation to the radial current density. The altitude r_0 should represent the "bottom" of the ionosphere at which no significant radial currents flow. However, as mentioned in the previous section, our technique relies on the assumption of treating the electrons as fully magnetized, so r_0 should be carefully chosen.

Another convenient property of the SECS basis functions for our purposes is that they have a short reach, and hence the model coefficients (the CF + DF SECS node amplitudes) are very localized in nature, describing the degree of divergence and curl of the vector field at their specific locations. In our layered description, each layer has a grid of CF and DF nodes. For simplicity we place the CF and DF nodes at the same locations within each layer, and use a grid that is approximately of equal area (Laundal & Reistad, 2022). In the vertical direction, the next layer has its nodes at the same spherical coordinates to simplify the vertical integration in equation 15. The resulting 3D grid is therefore a mesh with shape $(K \times I \times J)$, where the dimensions indicate the size in the vertical (K) and horizontal (I, J) dimensions. Since the ion-neutral interactions leading to perpendicular currents mainly take place in the E region, typically between 100 and 140 km, we use a closer spacing of the layers in this region. An example of the 3D grid can be seen in Figure 7. In this example grid oriented approximately towards magnetic north, 22 layers are used, starting at 90 km, with a 5 km separation up to 140 km. The horizontal resolution of the (17×11) element cubed sphere grid is (19×23) km with a total extent of (325×264) km in the (magnetic north, east) directions at the

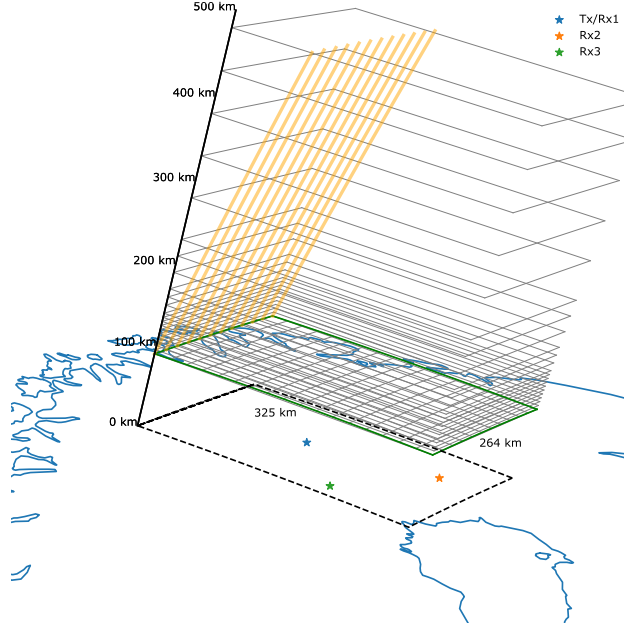


Figure 7. An example 3D grid using the proposed layered SECS representation. The altitude spacing is denser in the E region where \mathbf{j}_{\perp} has more structure. Magnetic field lines originating at the northern edge of the base of the grid is shown in orange to highlight the inclination above the E3D system. Note that the Tx/Rx sites shown here are not the real E3D sites, but the modified locations used in this paper.

base layer at 90 km. This leads to a total of $M = 2KIJ = 8,228$ SECS nodes to represent both the CF and DF fields in this case.

The numerical implementation is described in detail in Appendix A. This description is intended to complement the Python implementation of E3DSECS that is made publicly available (Reistad et al., 2024).

4 Performance of reconstruction technique

Figure 8 shows an example of the volumetric reconstruction of \mathbf{j} (bottom row) compared with the ground truth from the GEMINI model (upper row, no noise). Each spatial component is shown in separate columns, and 3 cuts are presented in each panel: One vertical cut in the central part of the volume (magnetic north-south direction), and two horizontal cuts at 102.5 and 355 km altitude. In this reconstruction we have included all the steps outlined above (using the velocity difference method to estimate \mathbf{j}_{\perp}) to try to assess the performance of the E3D radar system: A symmetric 31-beam configuration is used, and the covariances of the observed 3D ion velocities and electron densities along these beams are modelled using `e3doubt`, assuming a 10-min integration time during the fairly perturbed conditions in the GEMINI model run. We note that when evaluating the E3DSECS model, it is beneficial to evaluate on locations displaced half a grid cell in all 3 spatial directions, due to the singularities of the SECS elementary functions. This is done in all plots shown here.

The (r, θ, ϕ) components shown in Figure 8 refer to the geographic reference frame used in our representation. However, the orientation of the grid, and hence the vertical slice shown, corresponds approximately to the magnetic meridian, as the electrodynamic-

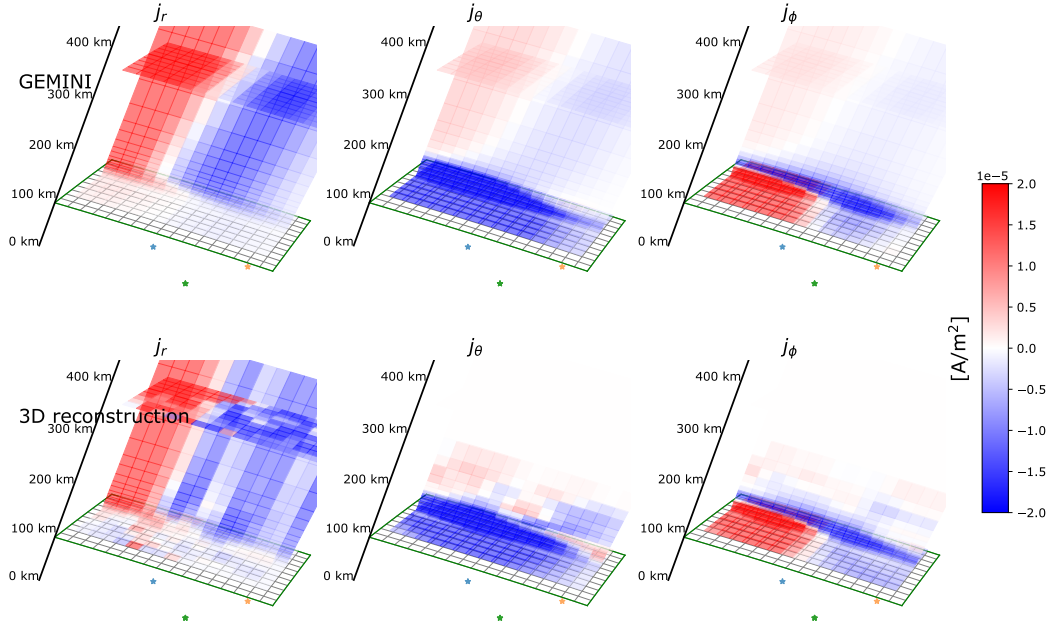


Figure 8. Example of how the proposed volumetric reconstruction technique performs shown on a vertical north-south slice through the domain, and two horizontal cuts at 102.5 and 355 km altitude. Top row: The ground truth that is sampled from (GEMINI model with no noise). The three columns show the r , θ and ϕ components of the full 3D current density vector. Bottom row: the corresponding estimated values from the volumetric reconstruction described above. Reconstruction of the horizontal components is overall better than the reconstruction of the radial component.

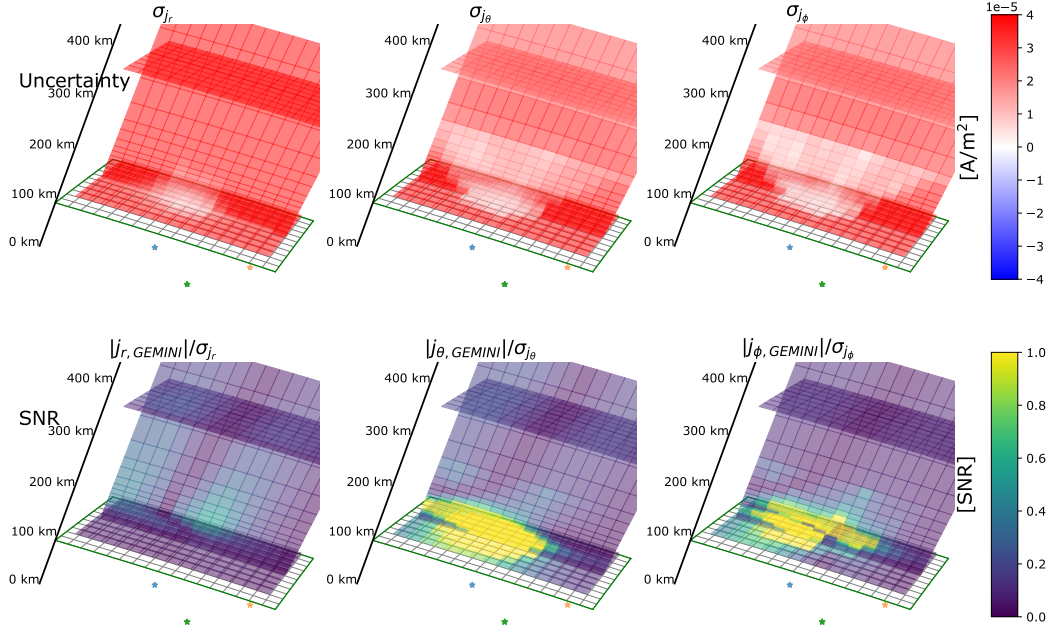


Figure 9. Top row: Current density vector component uncertainties (the square root of the diagonal of the 3D model covariance matrix propagated into 3D current density space). In addition to the vertical slice, two horizontal cuts are also shown. Bottom row: The ratio of the ground truth value of the current density component and the estimated uncertainty, highlighting the better ability to reconstruct the horizontal components compared to the vertical.

ics in the GEMINI simulation is forced with a pair of field-aligned currents (FAC) aligned north-south in magnetic coordinates, see Figure 2. In the GEMINI panels of the horizontal components a relatively weak current density is seen extending throughout the F region. This is the projection of the FACs into the horizontal components.

It is evident that especially the horizontal part of the reconstructed \mathbf{j} is a fairly accurate description of the ground truth in this case, in the E region. Above h_Φ at 200 km the model predicts negligible horizontal currents as no observations are provided here. However, despite the vertically connected horizontal layers of the CF part of \mathbf{j} , the vertical current density is more challenging to reconstruct on the basis of current continuity and the 31 beams used. This is expected as its value depends on an integral (sum) of the model parameters. Its large-scale features can be recognized, such as the transition from upward to downward FAC. It is evident that additional information would be beneficial to improve the 3D modelling capabilities of the vertical component of \mathbf{j} in this case.

Using the estimated covariance of \mathbf{j}_\perp based on realistic E3D sampling (equation 6) as the data covariance in equation A14, we get an estimate of the covariance of the modelled 3D current density \mathbf{j} . The square root of the diagonal elements of $cov(\mathbf{j})$, which we refer to as the "uncertainty," is shown using the same north-south and horizontal slices as earlier, in the upper row in Figure 9. It is clear that the radial component has the largest uncertainty, and that the uncertainty is reduced in the regions of dense measurements above the transmitter site below h_Φ . The bottom row in Figure 9 shows the ratio of the magnitude of the same current component from GEMINI, divided by the uncertainty in the top panel. This signal-to-noise ratio (SNR) type plot highlights where the estimated

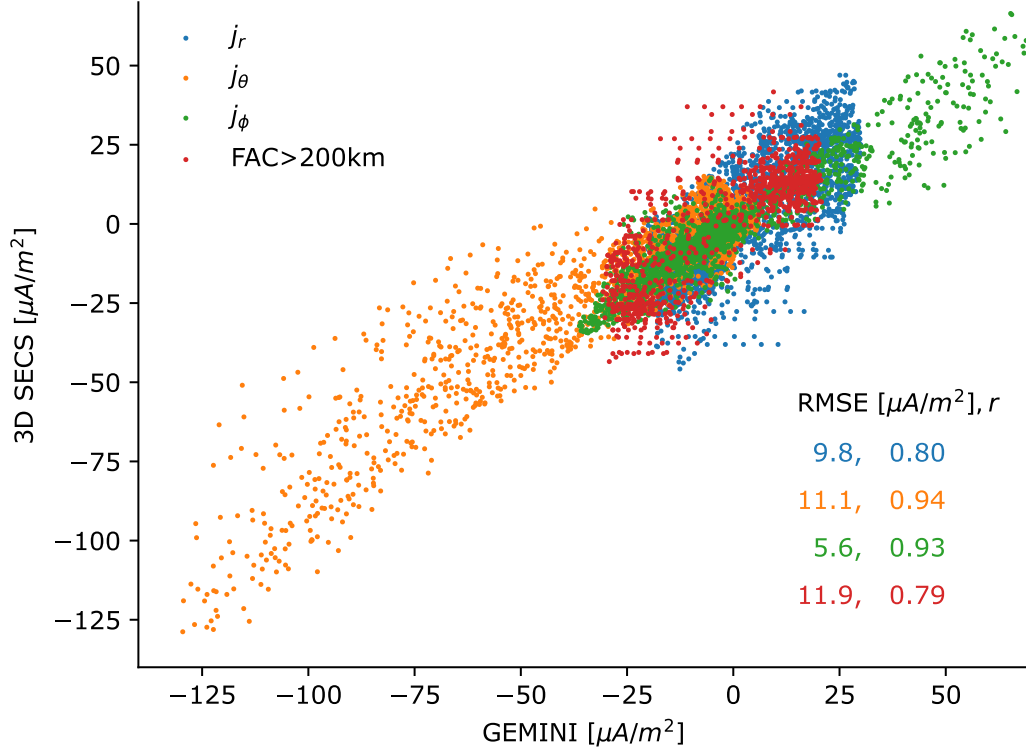


Figure 10. A different view of the performance of the 3D current density modelling, investigated by comparing the modelled values to the ground truth on a 3D mesh of points not used in the creation of the model. Again, the better performance of the horizontal components is seen. Colors represents the three components of \mathbf{j} , in addition to the field aligned component, as evaluated only above 200 km (red).

quantities can be expected to be good. This analysis suggests that in the regions of strong E region currents in the vicinity of E3D, the uncertainty of the 3D reconstructed horizontal components of \mathbf{j} is generally substantially less than the true value of the current density.

The performance of the 3D reconstruction is further investigated by comparing the model output on a uniform 3D mesh inside the domain (not the locations used to make the model) to the ground truth value from GEMINI. Figure 10 shows a scatter plot of each component of the current density, in addition to \mathbf{j} projected along the direction of the main magnetic field (FAC) for the evaluation locations above 200 km. Two different metrics of performance are also presented in Figure 10; the Root Mean Square Error (RMSE) and the linear correlation coefficient between the modelled and ground truth quantity. Despite having the smallest magnitudes among the three components, the radial component shows significant scatter, and has the lowest correlation value.

5 Strategies for improvements

The inverse problem of the volumetric reconstruction of the electric current density outlined in section 3 is typically under-determined, as is the case with the 31-beam experiment shown here. This section explores strategies to further constrain the problem, which could be possible in the application of this technique by incorporating ad-

ditional observations from other ground based and/or low-Earth Orbiting (LEO) instruments.

5.1 Specifying the field aligned current pattern on the top boundary

With large satellite constellations carrying magnetometers, like Iridium NEXT, the high latitude field-aligned current pattern is routinely monitored on a coarse scale. Furthermore, recent advances in regional ionospheric data assimilation like Lompe (Laundal et al., 2022; Hovland et al., 2022) significantly reduce the difficulty of utilising multiple observational sources to infer the mesoscale FAC pattern in a limited region.

We have explored the benefits on our 3D inversion scheme of specifying the radial current density on the top face of our domain (to be shown in Figures 11–13). This is implemented as additional observations when building the set of equations presented in equation A11. Additional rows are stacked, corresponding to the value of the radial current density in the centre locations of the upper layer of the grid, taken from GEMINI. These observations are related to the model parameters by constructing a corresponding \mathbb{S} matrix for those locations (see Appendix A), and we use a constant variance of $(1\mu A/m^2)^2$ for these observations in the inversion.

5.2 Specifying the vertical Hall and Pedersen current profile

Another strategy we have investigated is to impose prior knowledge of the vertical \mathbf{j}_\perp profile. Since we have here chosen to extend the 3D model above h_Φ , up to 500 km, the 3D model does not know that \mathbf{j}_\perp is assumed to be zero here, unless specified. We have tried to address this by adding a cost to the inversion based on a prescribed perpendicular current density profile above h_Φ . By relating the model amplitudes to the Pedersen and Hall current (found by projecting the modelled \mathbf{j}_\perp along $\hat{\mathbf{e}}$ and $\hat{\mathbf{b}} \times \hat{\mathbf{e}}$, respectively, where $\hat{\mathbf{e}}$ is the unit vector along the electric field), we add rows to \mathbb{G} in equation A11 of zero Hall and Pedersen currents along vertical profiles from each horizontal grid cell from 200 km and above, using a corresponding variance of $(1\mu A/m^2)^2$ in the inversion. This strategy can in principle be expanded using other types of observations, and will be discussed briefly in the next subsection.

5.3 Performance of improvement strategies

Figures 11–13 show the improvements on the volumetric reconstruction of \mathbf{j} by using the two additional constraints described above, in the same format as Figures 8–10. Comparing Figure 11 to Figure 8, the E region horizontal currents remain mostly similar. Above the E region, the additional constraints lead to predicted horizontal currents more similar to the projected part of the FAC as seen in the top row, indicating an improvement in this region. The vertical current density now has a structure that is more similar to the ground truth than earlier, as expected. A different view on the improvement in performance is seen by comparing the scatter plots in Figures 10 and 13. This confirms that the performance of the horizontal components is similar, with a marginal improvement of the performance metrics. Most significantly we observe that the radial and field-aligned components are significantly improved by the added constraints. We note that the specific noise from `e3doubt` that is added to \mathbf{v}_i and n varies each time we sample from the estimated distributions. Hence, the exact values in our plots change slightly between each realization of the noise, although the statistical properties are the same. However, the features we report here are representative trends for the performance, as we evaluate the model performance on $N = 3360$ locations in Figures 8–13, and have manually examined a handful of different realizations.

Similar to Figure 9, Figure 12 shows the estimated model parameter covariance propagated into current density space, shown as the square root of the diagonal elements of

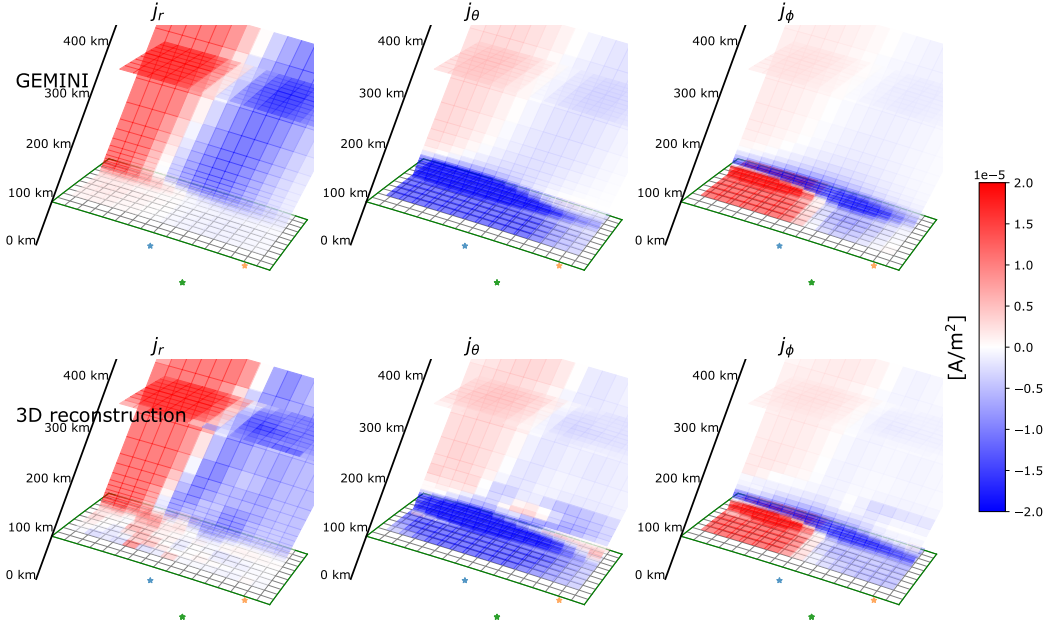


Figure 11. Performance of the 3D reconstruction when using the additional constraints described in sections 5.1 and 5.2. In the same format as Figure 8.

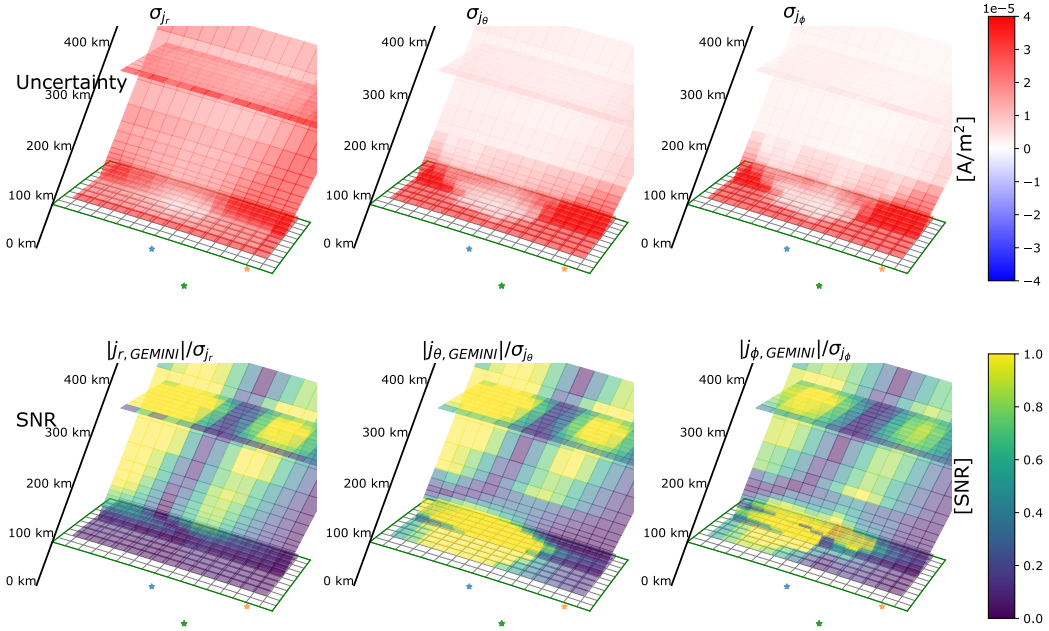


Figure 12. Uncertainties of the 3D reconstruction when using the additional constraints described in sections 5.1 and 5.2. In the same format as Figure 9.

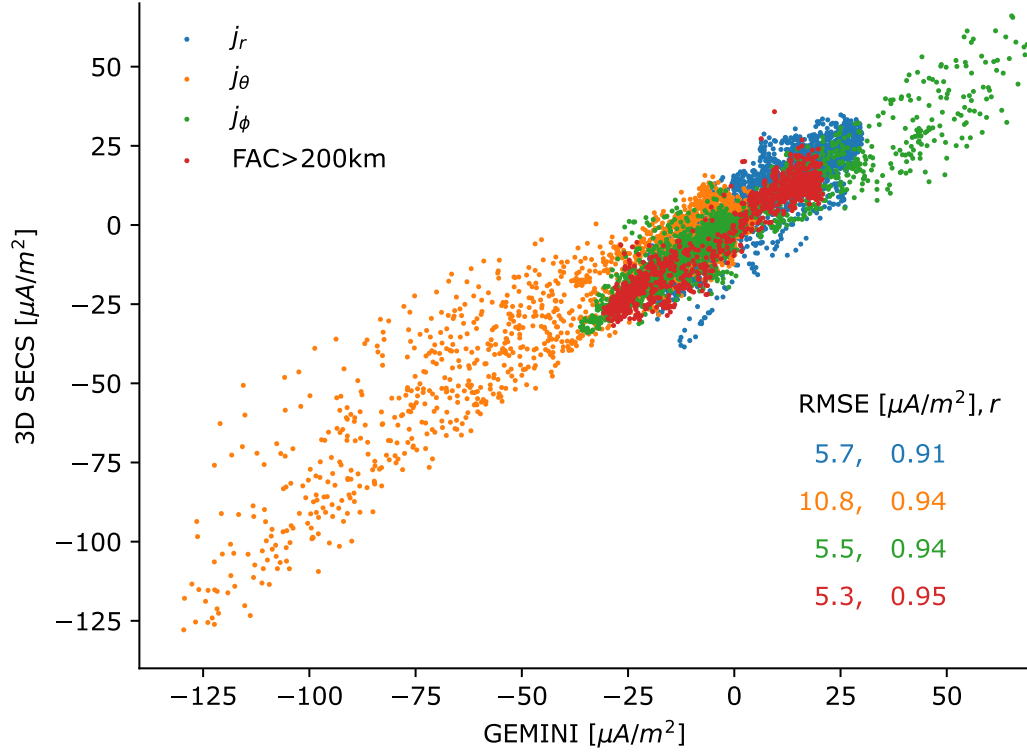


Figure 13. Performance of the 3D reconstruction when using the additional constraints described, in the same format as Figure 10.

$cov(\mathbf{j})$ in the same cuts as earlier. One can see that the uncertainty in the vertical component (σ_{j_r}) is now reduced across the vertical slice, and the corresponding SNR is ~ 1 in the F region, which is an improvement from Figure 9. σ_{j_θ} and σ_{j_ϕ} are also reduced, but mainly in the F region. This is due to the smaller influence on the solution from the E3D measurements when also the additional constraints are included in the fit. The strategy of adding information about the vertical profile of the current could also in principle be expanded, e.g. based on ionosonde data of the vertical electron density profile in combination with a model of the neutral atmosphere. Then the full altitude profile (not only starting at 200 km as done here) of the current could be imposed with a weight (variance) that must be determined, to inform the solution in regions void of E3D samples.

6 Concluding remarks

As outlined in section 5, one advantage of the direct physical meaning of the model parameters is the ability to relate them to other observations, like the radial current density at the top of the domain, and the Hall and Pedersen current, which could be inferred from other sources of data. In addition, the initial step outlined in section 2.3 is also very much suited to include additional data through the use of the Lompe framework. This includes data sources such as HF radars, ground and LEO magnetometers, all-sky cameras, and possibly F -region neutral wind estimates. Since the Lompe representation could provide both estimates of the horizontal height integrated Hall and Pedersen current as well as the field-aligned current, this can be used directly in the subsequent volumetric 3D reconstruction of \mathbf{j} , by formulating how the height integrated Hall and Pedersen currents in the 3D model relate to model parameters. This may further enforce the vertical coupling between layers for all model parameters (at present only CF parameters are directly linked through current continuity).

As mentioned in the introduction, the volumetric reconstruction of the electric field and neutral wind field by Stamm et al. (2023) represents a completely independent way of reconstructing the 3D ionospheric electrodynamics based on E3D measurements. The two approaches differ in the type of assumptions used, and the degrees of freedom in the representation of the electrodynamics. The framework presented here (E3DSECS) is designed to conveniently integrate additional data sources that describe the 3D electrodynamics, due to its strong similarities with the Lompe framework. It remains to be tested which of the formulations perform the best in various scenarios, possibly with simulated data like what is done in this paper (an OSSE).

Considering the estimates of the uncertainties of our volumetric reconstruction of \mathbf{j} , we suggest that our modelling approach could be feasible with E3D. However, it is likely that significant improvements can be made from including also additional data sources, especially in constraining the vertical component of \mathbf{j} . Ideally, better data coverage should help constraining all components of \mathbf{j} . However, we are also limited by the assumptions made in our formulation (e.g. the assumptions of ions and electrons being fully magnetised in different regions, and the steady state description of the convection electric field, $(\nabla \times \mathbf{E} = 0)$). The significant integration time needed to get acceptable covariances will also limit the ability to fit the data, as the system may evolve significantly during this time. In this paper we have not experimented extensively with the beam configuration to find an optimal pattern for this purpose. By optimising the beam pattern and operation mode of E3D, significant improvements are likely to be made in the performance of the volumetric reconstruction. Although the E3DSECS package together with `e3doubt` is suited for investigating this, the beam optimization task is not trivial and must be adapted to the specific scientific application of the experiment. We therefore deem this to be outside the scope of the present work. However, we mention some of the relevant considerations to take into account in the planning of such experiments: Lower elevation beams have generally increased noise levels because the beam width of the phased-array system increases with increasing zenith angle, making it difficult to reconstruct an extended

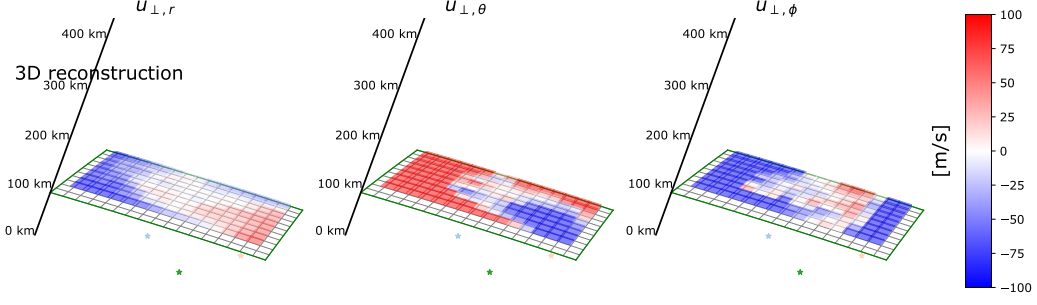


Figure 14. Neutral wind field components estimated directly via Equation 16. These estimates rely on \mathbf{j}_\perp obtained from the output of E3DSECS, \mathbf{E} from the initial step Lompe fit, and the ionospheric conductivities given from the GEMINI model.

horizontal region. Furthermore, the E-field mapping from F -region measurements may require additional beams than those used to sample the E region within the analysis volume, as the inclination of the B-field is such that the field lines at the southern edges of the 3D volume map out of the volume.

Using the velocity difference approach to estimate \mathbf{j}_\perp , one obtains current density estimates without making any assumptions about the neutral winds. Hence, Ohm's law (equation 2) can subsequently be used to infer the component of the neutral wind field perpendicular to \mathbf{B} , \mathbf{u}_\perp . The corresponding direct solution for \mathbf{u}_\perp given by rearranging Ohm's law is

$$\mathbf{u}_\perp = \frac{\mathbf{E} \times \hat{\mathbf{b}}}{B} + \frac{\sigma_h \mathbf{j}_\perp - \sigma_p \mathbf{j}_\perp \times \hat{\mathbf{b}}}{B(\sigma_p^2 + \sigma_h^2)}, \quad (16)$$

where B is the magnitude of the main field. \mathbf{E} is the electric field mapped down from the F region, not in the frame of the neutral wind. Figure 14 shows the three spatial components of \mathbf{u}_\perp at a horizontal cut at 102.5 km, using \mathbf{j}_\perp as described by our E3DSECS model, and mapping the topside E-field expressed by the Lompe-fit described in section 2.3. Furthermore, the Hall and Pedersen conductivities must be specified to carry out these estimates, here taken directly from the GEMINI model. In reality, this must be inferred from the E3D measurements through assumptions about the neutral atmosphere. In GEMINI, the neutral wind field is set to 0 m/s. Hence, the deviations from $\mathbf{u}_\perp = 0$ m/s reflect the uncertainties in estimates of \mathbf{u}_\perp with the proposed modelling scheme (not taking into account uncertainties in σ_H and σ_P that also must be estimated in the E3D case). It is clear that significant errors are seen outside the E3D beam pattern, agreeing with the error estimates of \mathbf{j} shown in Figures 9 and 12. However, within the region sampled by the E3D beams, the deviations from zero neutral wind are much smaller. In this limited region, approximately 50% of the grid cells in Figure 14 have absolute values < 30 m/s. Hence, we suggest that our volumetric reconstruction technique could be useful in producing maps of also \mathbf{u}_\perp in the E region above E3D.

Appendix A Numerical implementation

A python implementation with demonstration examples of the described 3D electric current model is made publicly available (Reistad et al., 2024). The following technical description aims at giving a complete description of how E3DSECS is implemented. We first explain in section A1 the most basic features and principles of the E3DSECS representation. Next, detailed information is provided in section A2 on how the different matrices are constructed. Section A3 brings together the different parts into the fi-

nal full set of equations, and section A4 describes how the solution is found through inversion.

A1 Core design principles of the relationship between \mathbf{j} and model parameters

What we infer from the E3D measurements is \mathbf{j}_\perp (see section 2.4), and what we want to reconstruct is the 3D current density \mathbf{j} everywhere in the domain. As outlined in section 3, the 3D representation of \mathbf{j} is described by SECS amplitudes. They are organized in an M -element column vector \mathbf{m} . The forward problem describing the linear relationship between the observations of \mathbf{j}_\perp and the model parameters \mathbf{m} is then

$$\mathbf{j}_\perp = \mathbb{G}\mathbf{m}. \quad (\text{A1})$$

Let's first assume that we only have 1 observation of $\mathbf{j}_\perp = (j_r, j_\theta, j_\phi)^T$. The matrix \mathbb{G} must necessarily contain the projection matrix (equation 13) which acts on the full current vector. Let's write this as

$$\mathbf{j}_\perp = \mathbb{B}\mathbb{G}'\mathbf{m}. \quad (\text{A2})$$

The matrix \mathbb{G}' must produce the 3D current vector \mathbf{j} from the set of model parameters \mathbf{m} , and must therefore have the shape $(3, M)$ for our single observation. Each row of \mathbb{G}' , when multiplied with \mathbf{m} , gives the corresponding component of \mathbf{j} . The first row of \mathbb{G}' , which corresponds to the radial component, must therefore involve the integral in equation 15.

We express the radial part as $j_r = \mathbb{S}\mathbf{m}$. \mathbb{S} is the matrix that carries out the integral in equation 15. When we only have 1 observation to relate, \mathbb{S} is $(1 \times M)$. More details on how \mathbb{S} is constructed is given in section A2. Next, let \mathbb{G}_h be the matrix that gives the two horizontal components of \mathbf{j} from the set of model parameters \mathbf{m} . \mathbb{G}_h will thus be made from the standard 2D SECS equations at each altitude layer (described in detail in section A2). When only one vector is calculated, it is a $(2 \times M)$ matrix. A full 3D current vector can then be calculated by

$$\mathbf{j} = \begin{pmatrix} j_r \\ j_\theta \\ j_\phi \end{pmatrix} = \mathbb{G}'\mathbf{m} = \begin{pmatrix} \mathbb{S} \\ \mathbb{G}_h \end{pmatrix} \mathbf{m} \quad (\text{A3})$$

In total, we then have

$$\mathbf{j}_\perp = \begin{pmatrix} j_{\perp,r} \\ j_{\perp,\theta} \\ j_{\perp,\phi} \end{pmatrix} = \mathbb{B} \begin{pmatrix} \mathbb{S} \\ \mathbb{G}_h \end{pmatrix} \mathbf{m}. \quad (\text{A4})$$

The next step is to expand these matrices so that we can calculate N \mathbf{j}_\perp vectors in one matrix multiplication, enabling the system of $3N$ equations to be inverted for \mathbf{m} .

A2 Details on how the different components of \mathbf{j} are related to \mathbf{m}

The matrices above produce only one vector. To map between the model parameters \mathbf{m} and N \mathbf{j}_\perp vectors we need to stack the vector components and the corresponding matrices in a specific way, as will be outlined in this and the following subsection. As mentioned above, we use divergence-free (DF) and curl-free (CF) SECS functions to describe the horizontal component of \mathbf{j} in K layers placed at the radial distance $r_{k=0,1,\dots,K-1}$. In each layer the functions are placed in a grid described by the coordinates θ_{ij}, ϕ_{ij} (same for all k), where $i = 0, 1, \dots, I-1$ and $j = 0, 1, \dots, J-1$. The location of each measurement n can be converted into the "k-i-j" coordinate space, i.e. each observation will have an exact (floating) value of its location in the 3D grid, (k, i, j) . Since we place the

SECS nodes in the centre of the voxels spanned by the (r, θ, ϕ) grid, its rounded number will refer to the specific grid cell the observation fall within. The exact value of the index will be used later in our implementation as a built-in (bi)linear interpolation feature, to take advantage of the knowledge of the exact location of the observation when coupling the horizontal layers. Unless otherwise stated, the kij indices refer to their rounded values. Furthermore, n and N , respectively, denote the n th observation and the total number of observations, and the superscript $*$ and \circ respectively refer to CF and DF parts.

Horizontal part of \mathbf{j}

The standard SECS matrices, \mathbb{G}_e^* and \mathbb{G}_n^* , produce the eastward and northward components of the CF current from a model vector at a set of N given coordinates (see e.g. Vanhamäki & Juusola, 2020). The 3D implementation described here stack these matrices from each layer in a specific way, as described here, using an existing SECS implementation (Laundal & Reistad, 2022) as a starting point. The size of \mathbb{G}_e^* and \mathbb{G}_n^* (and their DF counterparts) is $(N \times IJ)$ for each layer. Since the SECS nodes are located at the same (θ_{ij}, ϕ_{ij}) for all k , the SECS matrices at each layer (at radius r_k) will be the matrix at the bottom layer (r_0) multiplied by r_0/r_k . This holds also for the elements of the SECS matrices affected by the singularity correction described by Vanhamäki and Juusola (2020), which we also use. The model vector \mathbf{m} and the \mathbb{G}_h matrix must be constructed in a consistent manner through the stacking of the vertical layers. The stacking is done in the following way:

$$\mathbb{G}_m = \begin{bmatrix} -\mathbb{G}_{n,0}^* & \cdots & -\mathbb{G}_{n,K-1}^* & -\mathbb{G}_{n,0}^\circ & \cdots & -\mathbb{G}_{n,K-1}^\circ \\ \mathbb{G}_{e,0}^* & \cdots & \mathbb{G}_{e,K-1}^* & \mathbb{G}_{e,0}^\circ & \cdots & \mathbb{G}_{e,K-1}^\circ \end{bmatrix} \quad (\text{A5})$$

\mathbb{G}_m is a $(2N \times M)$ matrix describing the relationship between model parameters and the horizontal current density \mathbf{j}_h inside the 3D domain. This "k-i-j" stacking uses `numpy`'s `ravel/flatten/reshape` functions, called in the "k-i-j" order (using the row-major option), allowing convenient mapping between 1D kij and 3D (k, i, j) representations. We have chosen to let only the two closest layers to an observation describe its value. This means that all columns in \mathbb{G}_m not associated with `floor(k)` and `ceil(k)` will be zero, where k is the non-integer index of observation n in the vertical direction. Hence, at the two layers of interest for observation n , the altitude scaled SECS matrices are used, with a weight corresponding to the vertical distance of n from the two layers: $w_{\text{below}} = 1 - (k \bmod 1)$ for the below layer and $w_{\text{above}} = k \bmod 1$ for the above layer. All columns relating to model parameters in the rest of the layers will get a 0 value for the respective observation n . Hence, in this linear vertical weighting scheme, each row of \mathbb{G}_m will only have $4IJ$ non-zero values (IJ values for the layer above and below the measurement, for both the CF and DF amplitudes). Due to this "two-layer" implementation, only observations having $k \in [0, K-1)$ are considered. The "k-i-j" stacking of \mathbb{G}_h determines the order of the corresponding elements in the $(M \times 1)$ model vector: $\mathbf{m} = ((\mathbf{m}_{kij}^*)^T, (\mathbf{m}_{kij}^\circ)^T)^T$.

Radial part of \mathbf{j}

The calculation of j_r is done via the integral in equation 15. In this way, current continuity will be explicitly enforced, which will help to constrain the solution. Due to the grid design and SECS elementary function properties, we can approximate the integral as a sum to calculate j_r at \mathbf{r}_n :

$$j_r(\mathbf{r}_n) \approx - \sum_{q=0}^k \frac{m_{qij}^* (r_{q+1} - r_q)}{A_{qij}} \quad (\text{A6})$$

where \mathbf{r}_n is a position vector that points somewhere in the kij 'th grid cell and q is a sum index (in the vertical dimension) running up to the layer of observation n . It is evident that $j_r(\mathbf{r}_n)$ is a linear sum of the CF model parameters, each being proportional to the

divergence of the horizontal current density field inside its respective grid cell (see section 3.2). The negative sign is due to a positive divergence representing a current in negative $\hat{\mathbf{r}}$ direction. A_{qij} is the area of grid cell qij and m_{qij}^* is the curl-free SECS amplitude at that grid cell. Strategies for improving accuracy of the integration will be discussed in the next paragraph. Hence, the following expression in equation A7 is a slight simplification of what is actually used in the paper (see next paragraph). Based on equation A6, we can construct an $(N \times KIJ)$ matrix \mathbb{S} , whose elements are

$$S_{n,f(q,i_n,j_n)} = \begin{cases} -\frac{(r_{q+1}-r_q)}{A_{qin,jn}}, & q = 0, \dots, \text{floor}(k_n) - 1 \\ -\frac{w_{below}(r_{q+1}-r_q)}{A_{qin,jn}}, & q = \text{floor}(k_n) \\ -\frac{w_{above}(r_{q+1}-r_q)}{A_{qin,jn}}, & q = \text{ceil}(k_n) \\ 0, & q = \text{ceil}(k_n), \dots, K - 1. \end{cases} \quad (\text{A7})$$

$f(q, i_n, j_n)$ is a function returning the flattened index corresponding to the $qinjn$ 'th grid cell, which in our implementation is the `numpy.ravel_multi_index` function. k_n, i_n , and j_n are the indices corresponding to the grid cell of \mathbf{r}_n . In filling the columns of \mathbb{S} , q takes any integer value from 0 to $K - 1$ for each observation n . As evident from the above equation, the k index of observation n determines which expression to use when filling \mathbb{S} for each value of q . The above and below weights (w) are the same as used in the \mathbb{G}_m matrix. This weighting will act as a linear interpolation in the vertical direction when approximating the integral at a location between two SECS layers.

In the original SECS application (Amm, 1997), the SECS functions act as a 2D spatial interpolation scheme in between the nodes, and the modelled vector field can be smoothly reconstructed at any location (not taking into account possible singularity effects). While this is true for the horizontal part of \mathbf{j} , our above treatment of \mathbf{j}_r through current continuity does not lead to a similarly smooth \mathbf{j}_r field in the horizontal plane. This is due to the above integration being based solely on the SECS model amplitudes centered at the $(i_n j_n)$ 'th grid cells. Hence, any horizontal evaluation location inside that grid cell will yield the same result for j_r , making the horizontal variation of j_r pixelated, in comparison to the horizontal components of \mathbf{j} . We have implemented a simple bilinear interpolation scheme to avoid this. The idea is that for each observation, the radial integration is distributed among the four SECS nodes (at each layer) that the observation falls within. Equation A7 is still used to compute the elements, but in addition, there will be a 2D weight factor, $w_{2D}(i, j)$ multiplied to each element, depending on the location of n relative to the 4 neighboring CF SECS nodes. This leads to a smooth horizontal variation of the estimated j_r , based on the assumption of linear variation of the model amplitudes in the two horizontal directions.

A3 Full set of equations

If \mathbb{O} is a matrix of zeros with the same shape as \mathbb{S} , we now have that

$$\mathbf{j} = \begin{pmatrix} \mathbf{j}_r \\ \mathbf{j}_\theta \\ \mathbf{j}_\phi \end{pmatrix} = \begin{pmatrix} \mathbb{S} & \mathbb{O} \\ -\mathbb{G}_n^* & -\mathbb{G}_n^\circ \\ \mathbb{G}_e^* & \mathbb{G}_e^\circ \end{pmatrix} \begin{pmatrix} \mathbf{m}^* \\ \mathbf{m}^\circ \end{pmatrix} \quad (\text{A8})$$

The full matrix has dimension $3N \times M$ and represents a way to reconstruct the full 3D vector from knowledge about the horizontal components only, assuming current continuity and no vertical current at the bottom layer. This is the set of equations that is typically used in the forward problem when \mathbf{m} is known.

However, for the E3D application, we need to project the full 3D vector into the perpendicular direction since that is what can be estimated from the observations. To do that we have to stack the projection matrix \mathbb{B} from equation 13 in a way consistent with the component-wise $(\mathbf{j}_r, \mathbf{j}_\theta, \mathbf{j}_\phi)$ representation of \mathbf{j} in equation A8. To construct the

projection matrix for N observations, we use a permutation matrix \mathbb{P} that swaps the rows such that the components become sorted vectorwise, and then use that same permutation matrix to switch back after the projection has been performed. Renaming the \mathbb{B} matrices above as \mathbb{B}_n , corresponding to the n 'th observation (made from the magnetic field unit vector components at \mathbf{r}_n), we can make a full $3N \times 3N$ projection matrix like this:

$$\mathbb{B} = \begin{pmatrix} \mathbb{B}_1 & & & \\ & \mathbb{B}_2 & & \\ & & \ddots & \\ & & & \mathbb{B}_N \end{pmatrix} \quad (\text{A9})$$

where the rest of the matrix elements are zero. Since \mathbb{B} is now stacked so that it should operate on a $3N \times 1$ array of current vectors, sorted vectorwise and not componentwise, we make a permutation matrix (also $3N \times 3N$) like this:

$$\begin{aligned} \mathbb{P}_{3i,i} &= 1 \\ \mathbb{P}_{3i+1,i+N} &= 1 \\ \mathbb{P}_{3i+2,i+2N} &= 1, \\ i &= 0, 1, \dots, N-1, \end{aligned} \quad (\text{A10})$$

with zeros elsewhere. The transpose of this matrix is its inverse, and it performs the opposite permutation. The final relation between the components of \mathbf{j}_\perp as can be estimated with E3D and the model parameters \mathbf{m} is then:

$$\begin{pmatrix} \mathbf{j}_{\perp,r} \\ \mathbf{j}_{\perp,\theta} \\ \mathbf{j}_{\perp,\phi} \end{pmatrix} = \mathbb{P}^\top \mathbb{B} \mathbb{P} \begin{pmatrix} \mathbb{S} & \mathbb{O} \\ -\mathbb{G}_n^* & -\mathbb{G}_n^\circ \\ \mathbb{G}_e^* & \mathbb{G}_e^\circ \end{pmatrix} \begin{pmatrix} \mathbf{m}^* \\ \mathbf{m}^\circ \end{pmatrix} = \mathbb{G} \mathbf{m} \quad (\text{A11})$$

A4 Solving for the 3D model coefficients

Using the estimates of \mathbf{j}_\perp and its associated covariance, equation A11 can be solved for the model parameters \mathbf{m} .

$$\mathbf{m} = (\mathbb{G} \mathbb{C}_d \mathbb{G}^T + \lambda \mathbb{R})^{-1} \mathbb{G}^T \mathbf{d} \quad (\text{A12})$$

where \mathbb{C}_d is the data covariance matrix for the \mathbf{j}_\perp estimates as described by equation 6, λ is a zeroth order Tikhonov regularization parameter, \mathbb{R} is a regularization matrix described in the next section, and \mathbf{d} is the $(3N \times 1)$ column vector of the component-wise (r, θ, ϕ) observations of \mathbf{j}_\perp . Similar to equation 5, the covariance matrix of the 3D model vector is given by

$$\text{cov}(\mathbf{m}) = (\mathbb{G}^T \mathbb{C}_d^{-1} \mathbb{G} + \lambda \mathbb{R})^{-1} \quad (\text{A13})$$

Applying equation 4, the final covariance of the modelled 3D current density \mathbf{j} is then

$$\text{cov}(\mathbf{j}) = \text{cov}(\mathbb{G}' \mathbf{m}) = \mathbb{G}' \text{cov}(\mathbf{m}) \mathbb{G}'^T = \mathbb{G}' (\mathbb{G}^T \mathbb{C}_d^{-1} \mathbb{G} + \lambda \mathbb{R})^{-1} \mathbb{G}'^T. \quad (\text{A14})$$

where \mathbb{G}' is the matrix producing \mathbf{j} when multiplied with \mathbf{m} , see equation A8.

Regularization

Since the inverse problem is typically ill-posed, we need to apply regularization to get a meaningful solution. We employ a regularization scheme based on zeroth-order Tikhonov regularization (e.g. Aster et al., 2018) to encourage small model coefficients unless otherwise dictated by the data. The model amplitudes have a localized reach, are oriented in horizontal layers, and have units of A/m. They therefore represent the sheet current

density of the respective layer at their respective horizontal location. Since we use a variable vertical spacing of our layers to enable finer structures to be resolved in the E region, the conversion from the model coefficient values to horizontal current density values $[A/m^2]$ depends on the vertical spacing of layers at the point of interest. Since our data are in units of $[A/m^2]$, the zeroth order Tikhonov regularization parameter should reflect the differences in vertical spacing by being proportional to the vertical spacing distance for each parameter. Hence, the \mathbb{R} matrix in equations A12 - A14 is a diagonal $M \times M$ matrix whose diagonal elements are the vertical difference up to the next layer for each model parameter, where the last spacing is repeated for the top layer.

To find the optimal scaling value for \mathbb{R} (i.e. determining the value of λ), we use cross validation. Since we have a ground truth to compare with (GEMINI), we choose the value of λ that produces the smallest norm of the misfit vector, when the misfit is evaluated on a set of points from a uniform mesh that were not used to make the model (a test dataset). It should be noted that this is not directly applicable to E3D since the ground truth is not available, but the approach used here with synthetic data could potentially be used to choose λ in the case of real E3D data.

Appendix B Open Research

The implementation described in this paper is publicly available on GitHub (<https://github.com/jpreistad/e3dsecs>) and Reistad et al. (2024). Together with the GEMINI output used in this work for benchmarking and validation of the technique (Reistad & Zettergren, 2024), the code repository contains notebook scripts to perform the analysis and make all figures shown in this paper.

Acknowledgments

JPR and KML were funded by the Norwegian Research Council under contract 300844/F50, and SMH under contract 344061. MZ was supported by NASA grant 80NSSC21K1354. HV was supported by the Research Council of Finland project 354521. IV was supported by the Research Council of Finland project 347796. We also thank the Trond Mohn Foundation (SMH and KML) and the European Union (KML) through the ERC project DynaMIT under contract 101086985. This work benefited greatly from discussions during the International Space Science Institute (ISSI) International Team project #506 Understanding Mesoscale Ionospheric Electrodynamics Using Regional Data Assimilation.

References

- Amm, O. (1997). Ionospheric elementary current systems in spherical coordinates and their application. *J. Geomag. Geoelectr.*, *49*, 947-955. doi: 10.5636/jgg.49.947
- Amm, O., Grocott, A., Lester, M., & Yeoman, T. K. (2010). Local determination of ionospheric plasma convection from coherent scatter radar data using the secs technique. *Journal of Geophysical Research: Space Physics*, *115*(A3).
- Aster, R. C., Borchers, B., & Thurber, C. H. (2018). *Parameter estimation and inverse problems*. Elsevier.
- Boström, R. (1964, 12). A model of the auroral electrojets. *Journal of Geophysical Research*, *69*, 4983-4999. doi: 10.1029/jz069i023p04983
- Brekke, A., Doupnik, J. R., & Banks, P. M. (1974). Observations of neutral winds in the auroral e region during the magnetospheric storm of august 3–9, 1972. *Journal of Geophysical Research (1896-1977)*, *79*(16), 2448-2456. Retrieved from <https://agupubs.onlinelibrary.wiley.com/doi/abs/10.1029/JA079i016p02448> doi: <https://doi.org/10.1029/JA079i016p02448>
- Brekke, A., & Hall, C. (1988, August). Auroral ionospheric quiet summer time con-

- ductances. *Annales Geophysicae*, 6, 361-375.
- Fang, T.-W., Kubaryk, A., Goldstein, D., Li, Z., Fuller-Rowell, T., Millward, G., ... Babcock, E. (2022). Space weather environment during the spacex starlink satellite loss in february 2022. *Space weather*, 20(11), e2022SW003193.
- Farley, D. T. (1959, sep). A theory of electrostatic fields in a horizontally stratified ionosphere subject to a vertical magnetic field. *Journal of Geophysical Research*, 64(9), 1225-1233. Retrieved from <http://doi.wiley.com/10.1029/JZ064i009p01225> doi: 10.1029/JZ064i009p01225
- Hatch, S. M., & Virtanen, I. I. (2024). *EISCAT_3D Uncertainty Estimation (e3doubt)*. Retrieved from <https://github.com/Dartspacephysiker/e3doubt> doi: 10.5281/zenodo.10369301
- Hovland, A. Ø., Laundal, K. M., Reistad, J. P., Hatch, S. M., Walker, S. J., Madelaire, M., & Ohma, A. (2022, 12). The lompe code: A python toolbox for ionospheric data analysis. *Frontiers in Astronomy and Space Sciences*, 9. Retrieved from <https://www.frontiersin.org/articles/10.3389/fspas.2022.1025823/full> doi: 10.3389/fspas.2022.1025823
- Kaeppler, S. R., Hampton, D. L., Nicolls, M. J., Strømme, A., Solomon, S. C., Hecht, J. H., & Conde, M. G. (2015, 10). An investigation comparing ground-based techniques that quantify auroral electron flux and conductance. *Journal of Geophysical Research: Space Physics*, 120, 9038-9056. doi: 10.1002/2015JA021396
- Larsen, M. F. (2002, aug). Winds and shears in the mesosphere and lower thermosphere: Results from four decades of chemical release wind measurements. *Journal of Geophysical Research: Space Physics*, 107(A8), SIA 28-1-SIA 28-14. Retrieved from <http://doi.wiley.com/10.1029/2001JA000218> doi: 10.1029/2001JA000218
- Laundal, K. M. (2024). *Dipole - calculations involving dipole model of earth's magnetic field*. Retrieved from <https://github.com/klaundal/dipole>
- Laundal, K. M., & Reistad, J. P. (2022, February). *klaundal/secsy: secsy*. Zenodo. Retrieved from <https://doi.org/10.5281/zenodo.5962562> doi: 10.5281/zenodo.5962562
- Laundal, K. M., Reistad, J. P., Hatch, S. M., Madelaire, M., Walker, S., Hovland, A. Ø., ... Sorathia, K. A. (2022, 5). Local mapping of polar ionospheric electrodynamics. *Journal of Geophysical Research: Space Physics*, 127. Retrieved from <https://onlinelibrary.wiley.com/doi/10.1029/2022JA030356> doi: 10.1029/2022JA030356
- Laundal, K. M., Yee, J.-H., Merkin, V. G., Gjerloev, J. W., Vanhamäki, H., Reistad, J. P., ... Espy, P. J. (2021). Electrojet estimates from mesospheric magnetic field measurements. *Journal of Geophysical Research: Space Physics*, 126(5), e2020JA028644.
- Leadabrand, R. L., Baron, M. J., Petriceks, J., & Bates, H. F. (1972). Chatanika, alaska, auroral-zone incoherent-scatter facility. *Radio Science*, 7(7), 747-756. Retrieved from <https://agupubs.onlinelibrary.wiley.com/doi/abs/10.1029/RS007i007p00747> doi: <https://doi.org/10.1029/RS007i007p00747>
- Madelaire, M., Laundal, K., Gjerloev, J., Hatch, S., Reistad, J., Vanhamäki, H., ... Merkin, V. (2023). Spatial resolution in inverse problems: The ezie satellite mission. *Journal of Geophysical Research: Space Physics*, e2023JA031394.
- Madelaire, M., Laundal, K., Hatch, S., Vanhamaki, H., Reistad, J. P., Ohma, A., ... Lin, D. (2024). Estimating the ionospheric induction electric field using ground magnetometers. (Preprint. Available online at <https://doi.org/10.22541/essoar.170688756.62430384/v1>) doi: 10.22541/essoar.170688756.62430384/v1
- Maeda, K., & Kato, S. (1966). Electrodynamics of the ionosphere. *Space Science Reviews*, 5(1), 57-79. doi: <https://doi.org/10.1007/BF00179215>

- Mannucci, A. J., McGranaghan, R., Meng, X., & Verkhoglyadova, O. P. (2022, nov). An Analysis of Magnetosphere-Ionosphere Coupling That Is Independent of Inertial Reference Frame. *Journal of Geophysical Research: Space Physics*, 127(11). Retrieved from <https://onlinelibrary.wiley.com/doi/10.1029/2021JA030009> doi: 10.1029/2021JA030009
- Marklund, G. (1984). Auroral arc classification scheme based on the observed arc-associated electric field pattern. *Planetary and Space Science*, 32(2), 193-211. doi: [https://doi.org/10.1016/0032-0633\(84\)90154-5](https://doi.org/10.1016/0032-0633(84)90154-5)
- McCrea, I., Aikio, A., Alfonsi, L., Belova, E., Buchert, S., Clilverd, M., ... others (2015). The science case for the eiscat_3d radar. *Progress in Earth and Planetary Science*, 2(1), 1-63.
- Moen, J., & Brekke, A. (1993). The solar flux influence on quiet time conductances in the auroral ionosphere. *Geophysical Research Letters*, 20(10), 971-974. Retrieved from <https://agupubs.onlinelibrary.wiley.com/doi/abs/10.1029/92GL02109> doi: <https://doi.org/10.1029/92GL02109>
- Nozawa, S., Brekke, A., Maeda, S., Aso, T., Hall, C. M., Ogawa, Y., ... Fujii, R. (2005). Mean winds, tides, and quasi-2 day wave in the polar lower thermosphere observed in european incoherent scatter (eiscat) 8 day run data in november 2003. *Journal of Geophysical Research: Space Physics*, 110(A12). Retrieved from <https://agupubs.onlinelibrary.wiley.com/doi/abs/10.1029/2005JA011128> doi: <https://doi.org/10.1029/2005JA011128>
- Reistad, J. P., Laundal, K. M., & Hatch, S. M. (2024, February). *jpreistad/e3dsecs: First release of e3dsecs*. Zenodo. Retrieved from <https://doi.org/10.5281/zenodo.10682912> doi: 10.5281/zenodo.10682912
- Reistad, J. P., Laundal, K. M., Østgaard, N., Ohma, A., Haaland, S., Oksavik, K., & Milan, S. E. (2019). Separation and quantification of ionospheric convection sources: 1. a new technique. *Journal of Geophysical Research: Space Physics*, 124(7), 6343-6357.
- Reistad, J. P., & Zettergren, M. (2024, January). *GEMINI output used to develop volumetric reconstruction technique for EISCAT 3D*. Zenodo. Retrieved from <https://doi.org/10.5281/zenodo.10561479> doi: 10.5281/zenodo.10561479
- Richmond, A. D. (1995). Ionospheric electrodynamics using magnetic apex coordinates. *Journal of Geomagnetism and Geoelectricity*, 47, 191-212.
- Rishbeth, H. (1982). Europe probes the auroral atmosphere. *Nature*, 295, 93-94. Retrieved from <https://www.nature.com/articles/295093a0.pdf>
- Sangalli, L., Knudsen, D. J., Larsen, M. F., Zhan, T., Pfaff, R. F., & Rowland, D. (2009, apr). Rocket-based measurements of ion velocity, neutral wind, and electric field in the collisional transition region of the auroral ionosphere. *Journal of Geophysical Research: Space Physics*, 114(A4). Retrieved from <http://doi.wiley.com/10.1029/2008JA013757> doi: 10.1029/2008JA013757
- Stamm, J., Vierinen, J., & Gustavsson, B. (2021). Observing electric field and neutral wind with eiscat 3d. *Annales Geophysicae*, 39(6), 961-974. doi: <https://doi.org/10.5194/angeo-39-961-2021>
- Stamm, J., Vierinen, J., Gustavsson, B., & Spicher, A. (2023). A technique for volumetric incoherent scatter radar analysis. *Annales Geophysicae*, 41(1), 55-67.
- Vallinkoski, M. (1988). Statistics of incoherent scatter multiparameter fits. *Journal of atmospheric and terrestrial physics*, 50(9), 839-851. doi: 10.1016/0021-9169(88)90106-7
- Vanhamäki, H., Amm, O., & Viljanen, A. (2007). Role of inductive electric fields and currents in dynamical ionospheric situations. *Annales Geophysicae*, 25(2), 437-455. doi: 10.5194/angeo-25-437-2007
- Vanhamäki, H., & Juusola, L. (2020). Introduction to spherical elementary current systems. In M. Dunlop & H. Lühr (Eds.), (p. 5-33).

- 983 Zettergren, M. (2019, November). GEMINI: Geospace Environment Model
984 of Ion-Neutral Interactions [Computer software manual]. Retrieved from
985 <https://doi.org/10.5281/zenodo.3528915> doi: 10.5281/zenodo.3528915
986 Zettergren, M., & Snively, J. (2015). Ionospheric response to infrasonic-acoustic
987 waves generated by natural hazard events. *Journal of Geophysical Research:*
988 *Space Physics*, 120(9), 8002–8024.